



**Elisabete Luís Afonso Recuperação de elementos críticos de tecnologia
usando um nanocompósito à base de grafeno**

**Recovery of technology-critical elements using a
graphene based nanocomposite**



Elisabete Luís Afonso Recuperação de elementos críticos de tecnologia usando um nanocompósito à base de grafeno

Recovery of technology-critical elements using a graphene based nanocomposite

Dissertação apresentada à Universidade de Aveiro para cumprimento dos requisitos necessários à obtenção do grau de Mestre em Engenharia Química, realizada sob a orientação científica da Doutora Cláudia Maria Batista Lopes investigadora de pós-doutoramento do Departamento de Química da Universidade de Aveiro e coorientação científica do Doutor Carlos Manuel Santos da Silva, Professor auxiliar do Departamento de Química da Universidade de Aveiro.

o júri
presidente

Professora Doutora Inês Portugal
Professora auxiliar do Departamento de Química da Universidade de Aveiro

Doutora Cláudia Batista Lopes
Investigadora de pós-doutoramento do Departamento de Química da Universidade de Aveiro

Doutora Olga Manuela Matos de Freitas
Professora adjunta do Departamento de Engenharia Química do Instituto de Engenharia Química do Porto

agradecimentos

No decorrer desta dissertação de mestrado tive a oportunidade de desenvolver um trabalho inovador, que me permitiu crescer bastante a nível científico e também pessoal. No entanto, nada disto teria sido possível sem a ajuda e dedicação de todas as pessoas envolvidas, direta ou indiretamente nesta fase do meu percurso académico. Desta forma, deixo algumas palavras a quem eu gostaria de expressar o meu reconhecimento e agradecimento sincero.

À minha orientadora Doutora Cláudia Lopes, a ela devo o profundo agradecimento pelo modo como sempre me acompanhou e me apoiou ao longo deste trabalho. A incansável disponibilidade que sempre demonstrou, o apoio, a amizade e o seu vasto saber associado a um espírito crítico elevado, foram decisivos para a concretização desta dissertação e para o meu desenvolvimento científico e pessoal.

Ao meu coorientador Doutor Professor Carlos Manuel Silva, pelo seu incentivo, disponibilidade e pelas suas palavras amigas e sábias sempre no momento certo, bem como pela oportunidade que me deu de estar inserida no seu grupo de trabalho EgiChem.

À Professora Doutora Eduarda Pereira, agradeço a disponibilidade e apoio que sempre dispensou ao longo deste trabalho.

Ao Professor Doutor Tito Trindade pelo o apoio e por me ter disponibilizado o seu laboratório, o nanolab.

A todos os colegas do grupo EgiChem, do grupo da Química Analítica e Ambiental bem como do nanolab, agradeço a boa disposição, companheirismo e amizade, bem como o conhecimento transmitido e conselhos únicos que me ajudaram imenso no desenvolver desta dissertação.

Aos meus amigos que sempre me apoiaram e acompanharam neste grande percurso, pela amizade e carinho que sempre me transmitiram, um grande obrigada do fundo do coração.

Ao meu namorado João que sempre me ajudou e me apoiou, um grande obrigada pelos seus conselhos preciosos, pela paciência, amizade e carinho demonstrado durante este percurso.

Por último, um agradecimento muito especial à minha família em especial aos meus pais, pelo apoio incondicional e motivação, que me ajudaram a crescer e a seguir este percurso.

palavras-chave

Adsorção, Európio, Grafeno, Lantânio, Magnetite, Modelação, Nanocompósito, Térbio.

resumo

Os Elementos terras raras (ETR), inseridos no grupo dos elementos críticos de tecnologia, são definidos pela nomenclatura IUPAC como os 15 lantanídeos em conjunto com o ítrio e o escândio. Devido às suas propriedades únicas, os ETR podem ser utilizados em inúmeras aplicações de cariz tecnológico, o que tem contribuído para um aumento contínuo da sua procura. No entanto, a sua extração e processamento é um processo difícil e dispendioso, causando diversos problemas ambientais. Nesse contexto, uma alternativa, mais económica e amiga do ambiente ao atual processo de obtenção dos ETR, poderá passar pela sua recuperação de efluentes e rios, através de processos de separação, nomeadamente adsorção (e/ou permuta iónica). Esta técnica é bastante versátil, eficiente, simples e bastante adaptável. Nos últimos anos, o grafeno bidimensional, um dos mais recentes tipos de nanoestruturas de carbono, tem sido amplamente explorado numa vasta gama de aplicações. No entanto, o seu uso como adsorvente para recuperação de ETR tem sido pouco investigado. Por outro lado, os materiais magnéticos apresentam propriedades físicas e químicas únicas, com especial foco na química de superfície. Aproveitando os benefícios do grafeno e das nanopartículas de magnetite, nesta dissertação de mestrado será abordada uma estratégia simples, baseada em interações electrostáticas, para preparação de um nanocompósito magnético à base de grafeno (MG-bN). Após a síntese, o nanocompósito foi estudado como adsorvente para a remoção de três dos mais importantes ETR, lantânio (La(III)), európio (Eu(III)) e térbio (Tb(III)), em soluções aquosas mono elementares e ternárias através de experiências em descontínuo.

Os resultados revelaram que a adsorção de La(III), Eu(III) e Tb(III) pelo nanocompósito é muito sensível ao pH da solução e, as maiores percentagens de remoção ocorrem para valores de pH alcalinos. O nanocompósito em estudo apresenta uma rápida e elevada eficiência de adsorção, sendo que uma hora é suficiente para remover 82 % de Tb(III), 73 % de Eu(III) e 59 % de La(III) em soluções mono elementares com uma concentração inicial de 0.1 mg L^{-1} e utilizando apenas 50 mg L^{-1} de MG-bN. Já para soluções ternárias, a eficiência de remoção é um pouco mais baixa (30-58 %).

A cinética do processo de adsorção foi estudada usando três modelos cinéticos, nomeadamente os modelos de pseudo-primeira e pseudo-segunda ordem bem como o modelo de Elovich. O modelo de pseudo-segunda ordem foi o que apresentou um melhor ajuste aos valores experimentais para soluções mono elementares ($R^2 > 0.99$ e AARD < 5 %). Para soluções ternárias tanto o modelo de pseudo-segunda ordem como o de Elovich ajustam bem os dados experimentais ($R^2 > 0.99$ e AARD < 6%). Em todos os ensaios efetuados, o equilíbrio de adsorção foi ajustado pelo modelo de Langmuir e pelo modelo de Freundlich. A capacidade estimada do MG-bN para os elementos em estudo é maior em comparação com os valores relatados na literatura para outros adsorventes já estudados na recuperação dos mesmos elementos. A aplicação do MG-bN para a adsorção de lantânio, európio e térbio a partir de soluções aquosas confirma que este nanocompósito tem potencial para ser usado em sistemas de recuperação de elementos terras raras.

keywords

Adsorption, Europium, Graphene, Lanthanum, Magnetite, Modeling, Nanocomposite, Terbium

abstract

Rare-earth elements (REE), also known as Technology-critical elements, are defined by the IUPAC nomenclature, as the 15 lanthanides together with yttrium and scandium. Due to their unique properties REE can be widely used in many high-tech applications. The demand for REEs is continually growing, but mining and processing these elements are difficult, expensive and originate environmental issues. Due to their huge application, the presence of REE was recently detect in waste waters and rivers. Under this context, a cheaper and environmentally friendly alternative to obtain REE is the recovery of these elements from effluents and/or rivers by adsorption (and/or ion exchange). This technique is very versatile, efficient, has straightforward design and a wide adaptability.

In recent years, two-dimensional graphene, one of the newest type of carbon nanostructures has been extensively explored in a wide range of fields. However, its use as an adsorbent for REE recovery has been less investigated. On the other hand, magnetic materials are of considerable interest in material chemistry because of their unique physical and outstanding surface chemistry properties. Taking advantage of the combined benefits of graphene and magnetite nanoparticles, in this research a simple strategy based on electrostatic interactions, for preparing Fe_3O_4 /graphene based nanocomposite (MG-bN) is reported. The nanocomposite was then used as sorbent for the removal of lanthanum (La(III)), europium (Eu(III)) and terbium (Tb(III)), from single and ternary solutions, by carrying out batch experiments. Results have revealed that La(III), Eu(III) and Tb(III) uptake by the nanocomposite is very sensitive to solution pH and the highest efficiency occurs in alkaline media. The MG-bN shows fast and high adsorption efficiency, and 1 hour is sufficient to remove ca. 82 % of Tb(III), 73 % of Eu(III) and 59 % of La(III) from single solutions with an initial concentration of 0.1 mg L^{-1} and using only 50 mg L^{-1} of MG-bN. For ternary lanthanides solutions, the removal efficiency was lower (30-58 %).

The adsorption kinetics of the lanthanides was modelled by pseudo first-order Lagergren, pseudo-second order and Elovich models, three of the most well-known and widely applied kinetic models. The pseudo-second order model was the one that better describe the uptake process for unary solutions ($R^2 > 0.99$ e AARD < 5 %). For ternary solutions both pseudo-first order and Elovich models are the ones that better describe the uptake process ($R^2 > 0.99$ e AARD < 6%). The adsorption equilibrium was fitted by Langmuir and Freundlich isotherms. The estimated adsorption capacity of MG-bN for the lanthanides studied is higher than the values reported in literature for the sorption capacity of other adsorbents.

The application of the MG-bN for the uptake of lanthanum, europium and terbium from aqueous solutions confirms that this nanocomposite has potential to be used to recover rare-earth elements.

List of Contents

List of Figures.....	viii
List of Tables.....	x
Abbreviations.....	xi
1. Introduction	1
1.1. Technology-critical elements	1
1.2. Rare-earth elements	2
1.2.1. Chemical and physical properties	3
1.2.2. Supply, demand and applications	4
1.2.3. Rare-earth processing and its effects on environment and health	6
1.2.4. Alternative methods for recovery of rare-earth elements	8
1.2.5. Lanthanum, europium and terbium.....	10
1.3. Graphene materials.....	12
1.4. Objectives and outline of the thesis.....	14
2. Experimental.....	15
2.1. Synthesis and characterization of magnetic graphene-based nanocomposite	15
2.1.1. Exfoliation of graphite.....	15
2.1.2. Synthesis of magnetite nanoparticles.....	15
2.1.3. Preparation of the magnetic graphene-based nanocomposite.....	16
2.1.4. Characterization techniques.....	16
2.2. Adsorption experiments.....	17
2.2.1. Reagents.....	18
2.2.2. Glassware cleaning procedures.....	18
2.2.3. The effect of pH on the adsorption of La(III), Eu(III) and Tb(III) by the magnetic graphene-based nanocomposite	18
2.2.4. Kinetic experiments	19
2.2.5. Equilibrium isotherms experiments	20
2.3. Modelling	20
2.3.1. Kinetics modelling.....	20
2.3.2. Equilibrium isotherm modelling.....	22
3. Results and discussion.....	25
3.1. Characterization of magnetic graphene-based nanocomposite	25

3.1.1. Fourier transform infrared analysis	25
3.1.2. X-Ray diffraction analysis	26
3.1.3. Raman spectroscopy	27
3.1.4. Scanning transmission electron microscopy	28
3.1.5. Atomic absorption spectroscopy	30
3.1.6. Zeta Potential	30
3.1.7. Magnetic measurements.....	31
3.2. Adsorption of La(III), Eu(III) and Tb(III) by the magnetic graphene-based nanocomposite.....	32
3.2.1. Effect of pH.....	32
3.2.2. Kinetic studies.....	34
3.2.3. Equilibrium studies and modelling	43
4. Conclusions and future work.....	49
5. Publications and communications	51
Platform communication.....	51
Panel communication.....	51
References.....	53
Appendices	61
A- Magnetic nanocomposite fabrication	61
B- Adsorption experiments	62

List of Figures

Figure 1.1 - Technology-critical elements (in red) [2].	1
Figure 1.2 – United States Geological Survey for world mine reserves (USGS) estimates for rare earth oxides in United States, Australia, Brazil, China, India, Russia, Vietnam, other countries (Canada (0.7 %), Greenland (1.2 %), Malaysia (0.02 %), Malawi (0.1 %) South Africa (0.7 %)) [21].	5
Figure 1.3 - Carbon based nanomaterials: (a) graphite, (b) diamond, (c) nanoribbon, (d) graphene, (e) carbon nanotube, (f) fullerene [54].	12
Figure 1.4 - Some members of the graphene family: (a) graphene, (b) few-layer graphene, (c) graphite, (d) reduced graphene oxide (rGO), (e) graphene oxide (GO) [54].	13
Figure 3.1 - FTIR spectra of a) Fe_3O_4 NPs, b) graphite, c) EG and d) MG-bN.	26
Figure 3.2 - XRD patterns of a) graphite, b) EG, c) Fe_3O_4 NPs and d) MG-bN. The characteristic peaks of the samples are marked.	27
Figure 3.3 - Raman spectrum of a) graphite, b) EG, c) Fe_3O_4 NPs and d) MG-bN, showing the main Raman features, the D, G and 2D bands taken with a 532 nm excitation laser wavelength (1.0 or 0.1 mW).	28
Figure 3.4 - TEM (left) and SEM (right) images of graphite (a and b), EG (c and d), Fe_3O_4 NPs (e and f) and MG-bN (g and h).	29
Figure 3.5 - Calibration curve for AAS with 5 different iron standard solutions (0, 1, 2, 3, 4, 5 ppm).	30
Figure 3.6 - Zeta potential of MG-bN powders in NaCl aqueous solution at different pH values.	31
Figure 3.7 - Magnetization curves as a function of magnetic field for MG-bN. The right axis considers the estimated mass percentage of Fe_3O_4 which was determined using the Fe mass, and assuming that all magnetite is in perfect stoichiometry.	32
Figure 3.8 - Effect of pH on adsorption of La(III), Eu(III) and Tb(III) on MG-bN.	34
Figure 3.9 - Variation of normalized concentration and removal percentage of La(III), Eu(III) and Tb(III) from unary solutions (0.1 mg L^{-1}) with time, for different MG-bN concentrations. The bars represent the standard deviation. Experimental conditions: pH 7.7 ± 0.1 , mechanical stirring speed 500 rpm, MG-bN dose 10 mg L^{-1} (a and c) and 50 mg L^{-1} (b and d).	36

Figure 3.10 - Effect of contact time on the normalized concentration and removal percentage of La(III), Eu(III) and Tb(III) ternary solutions (0.1 mg L ⁻¹) by MG-bN adsorbent. The bars represent the standard deviation. Experimental conditions: pH = 7.7 ± 0.1, mechanical stirring speed 500 rpm, MG-bN dose 10 mg L ⁻¹ (a and c) and 50 mg L ⁻¹ (b and d). ¹	37
Figure 3.11 - Experimental and fitted data for: a) and b) La(III); c) and d) Eu (III); e) and f) Tb(III) using, respectively 10 and 50 mg L ⁻¹ of MG-bN, unary solutions. Experimental conditions: pH 7.7 ± 0.1 and room temperature ca. 25 °C. For clarity, error bars for La(III), Eu(III) and Tb(III) are omitted.	39
Figure 3.12 - Experimental and fitted data for: a) and b) La(III); c) and d) Eu (III); e) and f) Tb(III) using, respectively 10 and 50 mg L ⁻¹ of MG-bN, ternary solutions. Experimental conditions: pH 7.7 ± 0.1 and room temperature ca. 25 °C. For clarity, error bars for La(III), Eu(III) and Tb(III) are omitted.	41
Figure 3.13 - Experimental data and unary isotherms modelling of a) La(III), b) Eu(III), c) Tb(III) unary solutions onto MG-bN (pH 7.7 ± 0.1, initial concentration 0.1 mg L ⁻¹ and room temperature ca. 25 °C). Error bars are also presented.....	44
Figure 3.14 - Experimental data and multicomponent Langmuir isotherms and unary Freundlich isotherms for a) La(III), b) Eu(III), c) Tb(III) ternary solutions onto MG-bN (pH 7.7 ± 0.1, initial concentration 0.1 mg L ⁻¹ and room temperature ca. 25 °C). Error bars are also presented.....	47

Appendix A

Figure A. 1 - Preparation scheme of magnetic graphene based nanocomposite.	61
--	----

Appendix B

Figure B. 1 - Assembly scheme of adsorption experiments. a) fixed volume of lanthanides solution (500 mL), in 1000 mL two-necked round bottom flask; b) Ln ³⁺ solution with MG-bN; c) blank; d) sample collection for ICP-OES.	62
---	----

List of Tables

Table 1.1 - Applications of REE and their share in total demand [1], [5].....	6
Table 1.2 - Main characteristics of lanthanum, europium and terbium [7].	11
Table 3.1 - Optimized kinetic parameters obtained from pseudo-first order, pseudo-second order and Elovich models at pH 7.7 ± 0.1 , unary solutions (0.1 mg L^{-1} with MG-bN concentration of 10 mg L^{-1} and 50 mg L^{-1} . For comparison, the experimental q_{Ae} is shown.	40
Table 3.2 - Optimized kinetic parameters obtained from pseudo-first order, pseudo-second order and Elovich models at pH 7.7 ± 0.1 , ternary solutions (0.1 mg.L^{-1}) with MG-bN concentration of 10 mg L^{-1} and 50 mg L^{-1} . For better understanding, experimental q_{Ae} is also presented.....	42
Table 3.3 - Modelling results of adsorption isotherms of La(III), Eu(III) and Tb(III) for unary Langmuir and Freundlich isotherms.	45
Table 3.4 - Adsorption capacity for Eu(III) and Tb(III) of several materials used as sorbents in literature.	45
Table 3.5 - Modelling results of adsorption isotherms of La(III), Eu(III) and Tb(III) for multicomponent Langmuir isotherm and unary Freundlich isotherm.....	48

Abbreviations

AARD	Average absolute relative deviation
AAS	Atomic absorption spectroscopy
C_A	Concentration of adsorbate A, in solution, at time “ t ” (mg L^{-1})
C_{A0}	Initial concentration of adsorbate, A in solution (mg L^{-1})
$C_{A,e}$	Concentration of adsorbate A, in solution at equilibrium (mg L^{-1})
$\text{CuK}\alpha$	Copper K-alpha radiation for X-Ray diffraction analysis
DMF	N,N-dimethylformamide
EG	Exfoliated graphite
FTIR	Fourier-transform infrared spectroscopy
Fe_3O_4	Magnetite
GO	Graphene oxide
H_c	Coercive force
ICP-OES	Inductively coupled plasma optical emission spectroscopy
k_1	Rate constant of pseudo-first order adsorption (h^{-1})
k_2	Rate constant of pseudo-second order adsorption ($\text{g mg}^{-1} \text{h}^{-1}$)
K_F	Freundlich equilibrium constant ($\mu\text{g}^{1-1/n} \text{L}^{1/n} \text{g}^{-1}$)
K_L	Langmuir equilibrium constant (L mg^{-1})
n	Freundlich constant
NPs	Nanoparticles
M	Adsorbate
MG-bN	Magnetic graphene based nanocomposite
M_s	Saturation Magnetization
q_A	Amount of adsorbate sorbed at instant “ t ” (mg g^{-1}),
$q_{A,e}$	Amount of adsorbate sorbed at equilibrium (mg g^{-1}),
$q_{A,m}$	Maximum concentration of the adsorbed species when one complete monomolecular layer of coverage is achieved.
R^2	Coefficient of determination
REE	Rare-earth elements
rpm	Revolution per minute
S	Adsorption sites
S_{12}	Selectivity

SM	Concentration of adsorbate bound to the sorbent
STEM	Scanning transmission electron microscopy
T	Temperature (K/°C)
TCE	Technology-critical elements
V	Volume of solution (L)
W	Mass of the adsorbent material (g)
XRD	X-Ray diffraction analysis
Greek letters	
α	Initial adsorption rate in Elovich equation ($\text{mg g}^{-1} \text{h}^{-1}$)
β	Adsorption constant in Elovich equation (mg g^{-1})

1. Introduction

1.1. Technology-critical elements

In the past, there were a few trace elements that were considered just as laboratory curiosities but nowadays are key components for the development of new technologies. These elements are now called technology-critical elements and are of great relevance in the development of emerging key technologies such as renewable energy, electronics, energy efficiency or aerospace industry [1]. The name technology-critical elements (TCE) comes from the increasing use and demand of these elements for high-technology advancements, and at the same time due to their vulnerability to politically or economically driven fluctuations in supply [1], [2]. Currently, there is an international concern about ensuring their future supply, their costs, and the impacts this might have, so initiatives at all levels are underway to guaranty their availability in the coming years [2].

Depending on the source, the list of elements considered as TCE is available [1], [2]. According to Filella [2], technology-critical elements are presented in Figure 1.1, and include most of the rare-earth elements (REE), the platinum group elements, tantalum (Ta), niobium (Nb), gallium (Ga), germanium (Ge), indium (In), thallium (Tl) and tellurium (Te).

1 H Hydrogen																	2 He Helium	
3 Li Lithium	4 Be Beryllium											5 B Boron	6 C Carbon	7 N Nitrogen	8 O Oxygen	9 F Fluorine	10 Ne Neon	
11 Na Sodium	12 Mg Magnesium											13 Al Aluminum	14 Si Silicon	15 P Phosphorus	16 S Sulfur	17 Cl Chlorine	18 Ar Argon	
19 K Potassium	20 Ca Calcium	21 Sc Scandium	22 Ti Titanium	23 V Vanadium	24 Cr Chromium	25 Mn Manganese	26 Fe Iron	27 Co Cobalt	28 Ni Nickel	29 Cu Copper	30 Zn Zinc	31 Ga Gallium	32 Ge Germanium	33 As Arsenic	34 Se Selenium	35 Br Bromine	36 Kr Krypton	
37 Rb Rubidium	38 Sr Strontium	39 Y Yttrium	40 Zr Zirconium	41 Nb Niobium	42 Mo Molybdenum	43 Tc Technetium	44 Ru Ruthenium	45 Rh Rhodium	46 Pd Palladium	47 Ag Silver	48 Cd Cadmium	49 In Indium	50 Sn Tin	51 Sb Antimony	52 Te Tellurium	53 I Iodine	54 Xe Xenon	
55 Cs Cesium	56 Ba Barium	57 L Lanthanum	58 Hf Hafnium	59 Ta Tantalum	60 W Tungsten	61 Re Rhenium	62 Os Osmium	63 Ir Iridium	64 Pt Platinum	65 Au Gold	66 Hg Mercury	67 Tl Thallium	68 Pb Lead	69 Bi Bismuth	70 Po Polonium	71 At Astatine	72 Rn Radon	
87 Fr Francium	88 Ra Radium	89 A Actinium	90 Rf Rutherfordium	91 Db Dubnium	92 Sg Seaborgium	93 Bh Bohrium	94 Hs Hassium	95 Mt Meitnerium	96 Ds Darmstadtium	97 Rg Roentgenium	98 Cn Copernicium	99 Fl Flerovium		100 Lv Livermorium				
101 L Lanthanum		57 La Lanthanum	58 Ce Cerium	59 Pr Praseodymium	60 Nd Neodymium	61 Pm Promethium	62 Sm Samarium	63 Eu Europium	64 Gd Gadolinium	65 Tb Terbium	66 Dy Dysprosium	67 Ho Holmium	68 Er Erbium	69 Tm Thulium	70 Yb Ytterbium	71 Lu Lutetium		
102 A Actinium		89 Ac Actinium	90 Th Thorium	91 Pa Protactinium	92 U Uranium	93 Np Neptunium	94 Pu Plutonium	95 Am Americium	96 Cm Curium	97 Bk Berkelium	98 Cf Californium	99 Es Einsteinium	100 Fm Fermium	101 Md Mendelevium	102 No Nobelium	103 Lr Lawrencium		

Figure 1.1 - Technology-critical elements (in red) [2].

In this research, the target TCE under study are lanthanum, europium and terbium. These three elements belong to the REE group. The concept of REE, their main chemical and physical properties, their supply, demand and major applications as well as their production and related issues will be discussed in the following sections.

1.2. Rare-earth elements

The rare-earth elements, now considered as TCE, have been recognised for a long time as useful elements due to their distinctive chemical and physical properties [3]. The natural occurrence of REE depends strongly on the geological environment, and only in a few locations it is possible to find them in sufficient quantity and concentration, as well as in a suitable form and setting to make their extraction and exploitation economically viable [3].

The International Union of Pure and Applied Chemistry (IUPAC) defined rare-earth elements as the 15 lanthanides¹ from lanthanum to lutetium together with yttrium (Y) and scandium (Sc) [4]. These two elements are also considered REE, since they exhibit similar chemical properties to the lanthanides and tend to occur in the same ore deposits [5]. Rare-earth elements can be analysed as a single group due to their similar properties, although, various distinctions are often made. The most common is the division of REE in two sections: the light-group rare-earth elements (LREE), usually defined as lanthanum through gadolinium, and the heavy-group rare-earth elements (HREE), from terbium to lutetium, including scandium and yttrium [5], [6]. The line between LREE and HREE is not consistent among different authors, and sometimes the term ‘mid REE’ may also be used [7]. These two groups have differences in chemical properties, such as electron configuration and geological availability [5]. Rare-earth elements can also be divided according to the demand-and-supply: critical (Nd, Eu, Tb, Dy, Y and Er), uncritical (La, Pr, Sm and Gd) and excessive (Ce, Ho, Tm, Yb and Lu) [8].

¹ Lanthanum (La), Cerium (Ce), Praseodymium (Pr), Neodymium (Nd), Promethium (Pm), Samarium (Sm), Europium (Eu), Gadolinium (Gd), Terbium (Tb), Dysprosium (Dy), Holmium (Ho), Erbium (Er), Thulium (Tm), Ytterbium (Yb) and Lutetium (Lu).

1.2.1. Chemical and physical properties

The unusual properties of REE are mainly attributed to their atomic structure, in particular, to the configuration of their electrons, which is distinct from others elements [3]. Most of REE are lanthanides and have special electron configurations on the atomic level. In all elements, the atomic cores are surrounded by electrons on several orbitals and as the atomic number increases, protons, neutrons and electrons are gain. Usually, the electrons attach to the outer orbitals, but in the case of lanthanides is not the outer shell that is filled but instead a deeper lying orbital accommodates the new electron(s): the 4f orbital [7]. As the inner orbitals do not have a great influence on the chemical properties, and the outer orbital is the same for all lanthanides, the REE are chemically resemble [7]. On the contrary, this fact does not have the same influence on the physical properties, and different REE display different physical behaviours [7]. Another common characteristic of lanthanides is their trivalent oxidation state (Ln^{3+} , where Ln is the generic symbol for lanthanides). However, some REE may show other states (Ln^{2+} or Ln^{4+}). The preferred stable states are the ones that are attained by empty, half or full orbitals (e.g. La^{3+} (f^0), Gd^{3+} (f^7), Lu^{3+} (f^{14}), Eu^{2+} (f^7), Yb^{2+} (f^{14}), Ce^{4+} (f^0) and Tb^{4+} (f^7)) [7]. In addition, their chemical properties do not depend only on their atomic structure, but also on their size. Unusually, as the atomic number increases, the ionic radii gets smaller along a period (known as lanthanide-contraction), resulting in LREE and HREE occurring in different minerals [3]. This means that lutetium can substitute more readily other elements in minerals where the available sites are relatively small, and where the larger lanthanum ion will not fit.

Rare-earth elements usually form complexes dominated by electrostatic rather than covalent interactions, which are often very stable, as in the case of the oxides [9], [10]. Geologically occurring compounds tend to be oxides, halides, carbonates, phosphates and silicates, but not sulphides [3].

The solubility of REE can be influenced by two factors: chemical composition of the medium in which they are present in terms of speciation, and pH. For instance, field and laboratory experiments indicate that dissolved REE are affected by iron and aluminium colloid formation. Furthermore, some independent studies demonstrated that REE concentrations in water increase with decreasing pH [10]. A good knowledge in speciation and solubility of REE allows to evaluate the impact of REE presence in a variety of natural waters [10].

Regarding the physical properties, the REE show very diverse behaviours, making them very useful for a wide range of applications. Two of the most impressive properties of REE are the magnetism (e.g. Gd, Dy, Er, Nd and Sm show complex potentials useful for magnets fabrication) and phosphorescence (some REE provide sharply defined energy states, making them suitable for lighting and laser applications) [7].

In conclusion, there are important properties shared by all the REE, while others are specific to particular elements. Because of their chemical similarities, they occur together in minerals and rocks, and are difficult to separate from each other (known as “chemical coherence”) [3], making the REE extraction a technically complex process that requires intense processing. On the other hand, the numerous practical uses of REE often depend on physical properties (electrical, magnetic, spectroscopic, and thermal) which are specific to particular elements, highlighting the necessity of separating them.

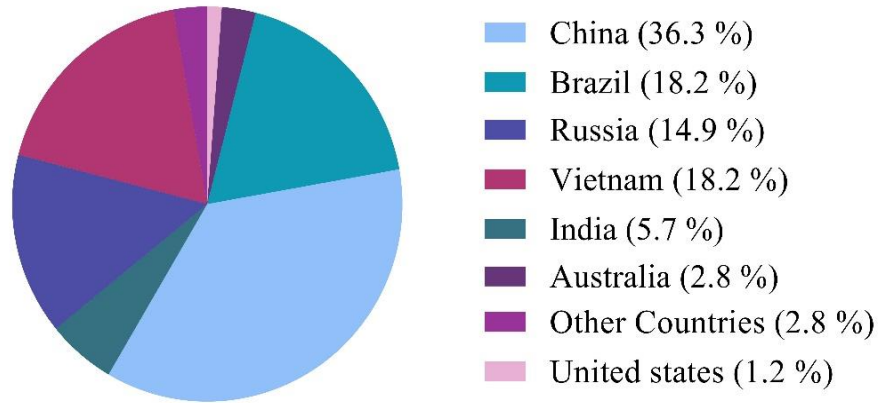
1.2.2. Supply, demand and applications

Some geochemical studies have revealed that the term *rare-earth elements* is a misnomer, because these elements are not rare in the Earth’s crust [7], [11], [12]. The two least abundant REE (Tm and Lu), for example, are nearly 200 times more common than gold. The term “rare” refers to the fact that these metals appear in the Earth crust (especially in exploitable ore deposits, such as bastnäsite, monazite, and xenotime) in lower concentrations than the other metals. Also, they do not naturally occur in metallic form, only as mixed and scattered in minerals [11], [13]. However, it is also noteworthy that in the Solar System, most lanthanides with an odd atomic number are actually lower, in abundance, than 94 % of the remaining elements, including Au, Pt, and other precious metals [14], [15], proving that REEs are rare, but at cosmic level.

Rare-earth elements are never found as pure metals, instead they are found in a variety of minerals [16]. Some studies [17]–[19] show that there are approximately 200 rare-earth minerals, but available minable concentrations are less common than for most other ores and so only few of them are economically viable to mine [12], [17]. Bastnäsite (a carbonate mineral), monazite (a phosphate mineral), and lateritic (ion-adsorption clays), which are aluminosilicate minerals are the primarily resources from where almost all production comes from today [9], [20]. Figure 1.2 shows the estimated reserves for China, Brazil, Russia,

Vietnam, India, Australia, United States and other countries (Canada, Greenland, Malaysia, Malawi and South Africa) in the year 2016 [21].

Global reserves, rare earth oxides (2016)



Total = 120.0 MT

Figure 1.2 – United States Geological Survey for world mine reserves (USGS) estimates for rare earth oxides in United States, Australia, Brazil, China, India, Russia, Vietnam, other countries (Canada (0.7 %), Greenland (1.2 %), Malaysia (0.02 %), Malawi (0.1 %) South Africa (0.7 %)) [21].

Unique properties, such as chemical, catalytic, magnetic, metallurgical and phosphorescence, make the possibility of REE to be applied in a wide range of fields. Today there are hundreds of uses for REE, ranging from high tech (lasers, camera lenses, computer memory modules, x-ray machines), energy (batteries, lamps, superconductors) and other industrial applications (aerospace, caustic cleaning agents, specialized glass) [1], [5], [11]. Table 1.1 shows some of these applications.

Table 1.1 - Applications of REE and their share in total demand [1], [5].

Rare-earth elements	Group of applications	Type of products	Share in total demand for REEs (economic value)
Nd, Pr, Tb, Dy	Magnets	Smartphones, optical drives, hard disc, wind turbines, electric/hybrid vehicles	37 %
Eu, Y, Ce, Gd, Tb, La	Phosphors and luminescence	Displays, LED, lamps	32 %
La, Ce, Pr, Nd	Metal alloys/batteries	NiMH batteries, fuel cells	14 %
Ce, La, Y	Glass, polishing and ceramics	Colouring and decolouring agents in glass	9 %
Ce, La	Catalysts	Automotive& chemical process catalysts.	5 %

1.2.3. Rare-earth processing and its effects on environment and health

The processing of rare-earth and the latter separation of the individual REE are important but complex tasks that require both physical and chemical treatments [7]. The production of REE can be described in four main steps: mining, physical beneficiation, extraction of oxide products and separation of individual REE [7]. The acquisition of most REE starts by mining the natural environment [17], [18]. This, like the majority mining operations, results in a large quantity of excess and unused materials and a lot of environmental issues associated. Depending upon the deposit type, different rare-earth contents are present and so different mining methods are use (leached *in situ*, underground or open pit) [18]. For example, if the deposit type is mineral and sand based monazite, wet-dredging or dry mining method² is applied. On the other hand, if it is hard rock based type then conventional open-cut or underground truck shovel mining system³ is used [10]. Hence, for a typical open pit mine,

² Wet-dredging is a process to remove sediment from underwater [103] and dry mining is used to separate and recover metals and minerals concentrate in dry mode without the use of water, is a process where is no moisture in the ventilating air [104].

³ Underground truck shovel mining process is the most flexible mining method [105].

removal of overburdened, mining, milling, crushing and grinding are involved. In this process (physical beneficiation), the product of the enriched concentrate after separation may contain around 30 % to 70 % of rare-earth bearing ore. This step requires high amounts of water and energy usage as well as production of waste streams (tailings and wastewater) [22], [23].

After mining, further processing and refining are required to extract REE. Typically, the extraction process involves the use of acidic or alkaline routes, depending on the mineralogy of the elements-containing phases and reactivity of gangue⁴. Approximately 90 % of the extraction methods is done by acidic route [23]. This normally involves roasting the REE at 400-500 °C in concentrated sulfuric acid to remove CO₂ and fluoride, and to change the mineral phase (roasting in such conditions make the REE more water soluble) [23]. The REE are then further leached using extraction and precipitating agents. After that, it is necessary to proceed to the individual REE separation process. The separation of REE can be carried out by different methods (fractional crystallization, fractional precipitation, ion exchange and solvent extraction), taking advantage of the small differences in basicity resulting in a decrease of the ionic radius from lanthanum to lutetium [7]. In practical, these basicity differences have influence on the properties (solubility of salts, the hydrolysis of ions, and formation of complex species) that are the basis of the separation procedures mentioned above [7].

In general, producing, processing and then disposing of REE have environmental and health issues associated. The handling of chemicals before, during and after processing, together with the radioactive materials storage of some tailings, are the main environmental problems associated to REE production [3] posing real threat to environment as well as occupational and public safety and health risks.

In this field, literature is mostly confined to reports on lanthanum and cerium, with little knowledge about of the health issues associated to other REE [10], [24]. There are some adverse outcomes of REE exposure including growth inhibition, oxidative stress, cytogenetic effects, and organ-specific toxicity [24]. Most REE metals are considered mildly to moderately toxic.

⁴ Gangue is defined as the minerals that surrounds, or are closely mixed with, a wanted mineral in an ore deposit [106].

Among lanthanum, europium and terbium, lanthanum is the most dangerous in the working environment, because damps and gasses can be inhaled with air. This can cause lung embolisms and lung cancer during long-term exposure [10]. When accumulated in the human body, it can originate liver diseases [22], [25]. When released in the environment, lanthanum will gradually accumulate in soils leading to increasing concentrations in soil particles, humans and animals [10].

In literature, little information is available regarding europium and terbium toxicity effects. It is known that europium has no known biological role compared to other high-density metals, although their toxicity has not been investigated in detail. However, it is known that dust from its metal compounds has fire and explosion hazards. As compared to other lanthanides, terbium compounds have low to moderate toxicity. However, in contact with the skin and eyes, Tb can be very irritating. No environmental threat to plants or animals are known [10], [26], [27].

The environmental issues associated with REE may be addressed at several stages, such as mining and refining, transportation, processing, waste disposal and decommissioning. This will cause negative effects in aquatic and terrestrial organisms, as well as in human [10].

1.2.4. Alternative methods for recovery of rare-earth elements

Until now, mining and processing activities are the main ways to obtain REE. However, as mentioned previously, these activities can be very dangerous for the environment and people's health, and some elements have relatively low abundance which raises to economic issues⁵, highlighting the need for alternative methodologies to obtain REE.

So far, the presence of REE in rivers, wastewaters and effluents was typically in ultra-trace concentrations, due to the absence of any significant industrial role prior to their massive use in the increasing demand of new technological applications. However, this scenario is changing rapidly and substantially. The current use of REE in new technological products is resulting in significant changes in the processes associated with their natural environmental cycle at the Earth's surface due to increased mining activities and use in a variety of products. Currently, at all stages of their life cycle, these elements and their compounds can be released into the environment, and there are already some works that

⁵ Some REEs are very expensive due to their low abundance and costs associated to their extraction, leading to economic issues.

reported the presence of REE in rivers and wastewaters [28]–[30], as well as in solid wastes [29]. These solid wastes and streams could become economically attractive secondary sources of REE, and thus, there is an opportunity window to develop methodologies for the efficient recovery of REE from waters and wastewaters, mitigating the hazardous consequences of the mining process.

Recently, some studies have been driven in that direction. For instance, Carvalho et al [31] reported a method for the recovery of Eu(III) from water with concentration of 0.0152 g L^{-1} , using magnetite nanoparticles (NPs). In this paper magnetite NPs showed a high potential, as nanosorbents for the uptake of lanthanide ions dissolved in water at pH 7. The authors also applied surface modification of Fe_3O_4 NPs, which led to an improvement of the removal capacity of the sorbents when used at pH close to neutrality $q_{A,m}=32.6 \text{ mg g}^{-1}$ for $\text{Fe}_3\text{O}_4@\text{SiO}_2/\text{APMS}$. Sun et al. [32] synthesized and characterized graphene oxide nanosheets for the removal of trivalent lanthanides and actinides from large volumes of aqueous solutions. The authors achieved at pH 6 and $T=298 \text{ K}$ the maximum adsorption of Eu(III) on GO nanosheets which was calculated to be 175 mg g^{-1} for a high initial lanthanide concentration ($\sim 51 \text{ mg L}^{-1}$). They also proved that the ionic strength had no effect on Eu(III) adsorption. In conclusion, Sun et al [32] showed that GO nanosheets are a suitable material for the preconcentration and removal of trivalent lanthanides and actinides from aqueous solutions in environmental pollution management. Gabor et al. [33] developed an adsorbent based on magnesium silicate functionalized with tetrabutyl ammonium for La(III) removal from aqueous solutions. With this adsorbent material, the authors achieved the optimum contact time of 15 minutes ensuring a $\sim 95 \%$ La(III) removal efficiency at 298.15 K for a sorbent dose of 4 mg L^{-1} and metal concentration of 1 g L^{-1} . Ponou et al [34] reported a biosorption method using carbonized ginkgo leaves. The authors reported that at pH 3 and after 900 s, the recovery of the lanthanides in study was of 95 % and the maximum adsorption of La, Ce and Er were calculated to be, 0.055 ± 0.019 , 0.085 ± 0.007 .and $9.910 \pm 0.172 \text{ mg g}^{-1}$, respectively.

The recovery of REE from old mine tailings, industrial wastewater streams or even from rivers is still in its beginning (mainly since the concentrations of these elements are low in comparison to the primary rare-earth ores), but special processes dedicated to the recovery of REE from these dilute waste streams need to be developed and will be certainly a hot topic in the near future.

1.2.5. Lanthanum, europium and terbium

In this research, the target TCE under study were lanthanum, europium and terbium. The selection of these elements was due to their importance and to some dissimilarities since usually they are classified as: lanthanum a LREE, europium a MREE and terbium a HREE.

Lanthanum (La) is a REE of Group 3 in the periodic table, this element is the archetype of the lanthanides. There are three allotropic (structural) forms of La: the α -phase (double close-packed hexagonal), β -phase (face-centred cubic) and the γ -phase (body-centred cubic). Lanthanum is a soft (that can be cut with a knife), ductile, malleable silver white metal [35]. When exposed to air and at room temperature lanthanum rapidly oxidizes to form La_2O_3 . It is the highest electropositive element from the lanthanide group. From 6 K to its melting point (1191 K) with a nearly temperature-independent magnetic susceptibility between 4 and 300 K, the metal is paramagnetic⁶ [35], [36]. Pure lanthanum has a very few applications (almost limited to the scientific research), but when is added to other elements such as oxygen, hydrogen, sulphur or ferrous alloys, cleaner metals are obtained and the number of applications increases. For example, La is used as a catalyst, additive in glass, scintillator, electron cathode, ignition element in lighters and torches and in carbon lighting for studio lighting and projection [37].

Europium (Eu) was discovered in 1901 by Eugène-Anatole Demarçay, a French chemist [38]. This element is the softest, the least dense, the most volatile and the most reactive member of the lanthanide series. When pure this metal is silvery, but when exposed to air it becomes dull⁷. Europium has two stable isotopes: ^{151}Eu that is used to produce ^{152}Eu , and the other one is ^{153}Eu . These isotopes are good neutron absorbers. The principal ores containing europium are bastnäsite and monazite (also it has been identified spectroscopically in the sun and others stars) [39]–[42]. Usually europium is separated from the other REE by reducing it to the +2 oxidation state and precipitating it with sulphate ions. This element can be found as a single allotropic (structural) form with a body-centred cubic structure. It can be used in red phosphors in optical displays and TV screens that use cathode-ray tubes and in glass for fluorescent lamps. Also it can be used as a source of blue colour in light-emitting diodes (LEDs) and in scintillators for X-ray [40], [42].

⁶ Paramagnetic materials have unpaired electrons, resulting in a positive magnetic susceptibility. These materials become magnetized in a magnetic field but their magnetism disappears when the field is removed.

⁷ When exposed to the air, europium readily oxidizes to form $\text{Eu}(\text{OH})_2 \cdot \text{H}_2\text{O}$.

Terbium (Tb) was discovered in 1843 by Carl Gustaf Mosander [43]. Terbium is a silver-grey metal, ductile, malleable and soft enough to be cut with a knife [43]. When in pure form, the metal is stable in air, even at high temperatures. The oxide is a chocolate or dark marron colour. Terbium is found in cerite, gadolinite and other rare-earth minerals, but it is recovered commercially from monazite (in which it is present to the extent of 0.03 %), xenotime, and from euxenite (a complex oxide containing 1 % or more of terbia⁸). The only natural isotope of the element is ¹⁵⁹Tb, but it was found a total of 36 (excluding nuclear isomers⁹) radioactive isotopes of terbium. Terbium is one of a few REE that have +4 as well as +3 oxidation states, this is due to the stability of the half-filled 4f shell. Terbium is used to dope calcium tungstate, calcium fluoride and strontium molybdate and can be applied in colour phosphors in lighting applications such as trichromatic lighting and in colour TV tubes. It is also used to make green colour on high definition screens [26], [42], [44].

Table 1.2 shows the main characteristics of lanthanum, terbium and europium.

Table 1.2 - Main characteristics of lanthanum, europium and terbium [7].

Element	La	Eu	Tb
Atomic Number	57	63	65
Expected electronic configuration (Ln)	[Xe] 4f ⁰ 5d ¹ 6s ²	[Xe] 4f ⁶ 5d ¹ 6s ²	[Xe] 4f ⁸ 5d ¹ 6s ²
Observed electronic configuration (Ln ³⁺)	[Xe] 4f ⁰ 5d ¹ 6s ²	[Xe] 4f ⁷ 5d ⁰ 6s ²	[Xe] 4f ⁹ 5d ⁰ 6s ²
Oxidation states	+3	+2	+3
		+3	+4
Colour	colourless	nearly colourless	nearly colourless
Atomic radius (pm)	187	204	178
Ionic radius (pm)	103	95	92
Atomic mass (u)	138.9	152.0	158.9
Mass in geosphere	0.002	10 ⁻⁵	9×10 ⁻⁵
Boiling point (K)	3730	1870	3396
Melting Point (K)	1194	1095	1629
Density (kg m ⁻³)	6145	5243	8229

⁸ Terbia is the rare earth terbium oxide, Tb₂O₃.

⁹ The nuclear isomers of Tb are 27 in number, and Tb-156m is the most stable isomer [27]

1.3. Graphene materials

In recent years, due to their unique properties, nanomaterials have emerged as a new type of adsorbent for distinct applications in water treatment [45]–[48]. Size effects and the increased fraction of “surface” atoms result in the change of physical and chemical properties of these small materials [48]. These atoms on the surface normally have high chemical activity and adsorption capacity, making nanomaterials good adsorbents compared to classic solids¹⁰ [49]. In this field, carbon-based nanomaterials (Figure 1.3) play an important role and have attracted the scientific community since they are known [50]–[53].

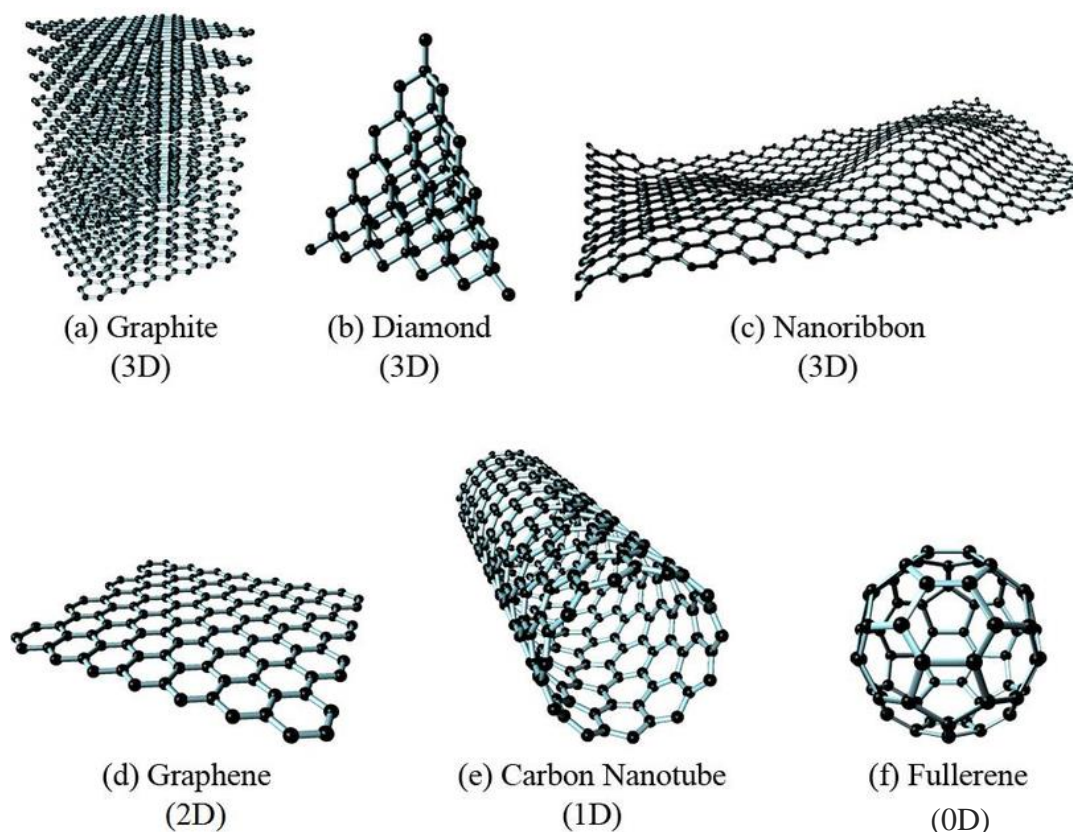


Figure 1.3 - Carbon based nanomaterials: (a) graphite, (b) diamond, (c) nanoribbon, (d) graphene, (e) carbon nanotube, (f) fullerene [54].

Graphene, an emerging class of carbon materials, has been extensively explored due to its enormous potential in a wide range of fields, including composite materials, transparent electrodes, gas sensors and transistors [55], [56]. Graphene, an allotrope of carbon, is a one-atom layer tightly packed in a hexagonal honeycomb sp^2 carbon lattice. It is one of the newest type of carbon nanostructures. Related materials include few-layer graphene, ultrathin graphite, graphite nanoplates, graphite nanosheets, graphite nanoflakes, exfoliated

¹⁰ Activated carbon and alumina are called classical substances.

graphite, graphene quantum dots, graphene oxide (GO), reduced graphene oxide (rGO), and graphene nanosheets [54], [57]. Some of these graphene related materials are presented in Figure 1.4. These materials vary in layer number, surface chemistry, lateral dimension, defect density, purity, composition and also quality of the individual graphene sheets [57].

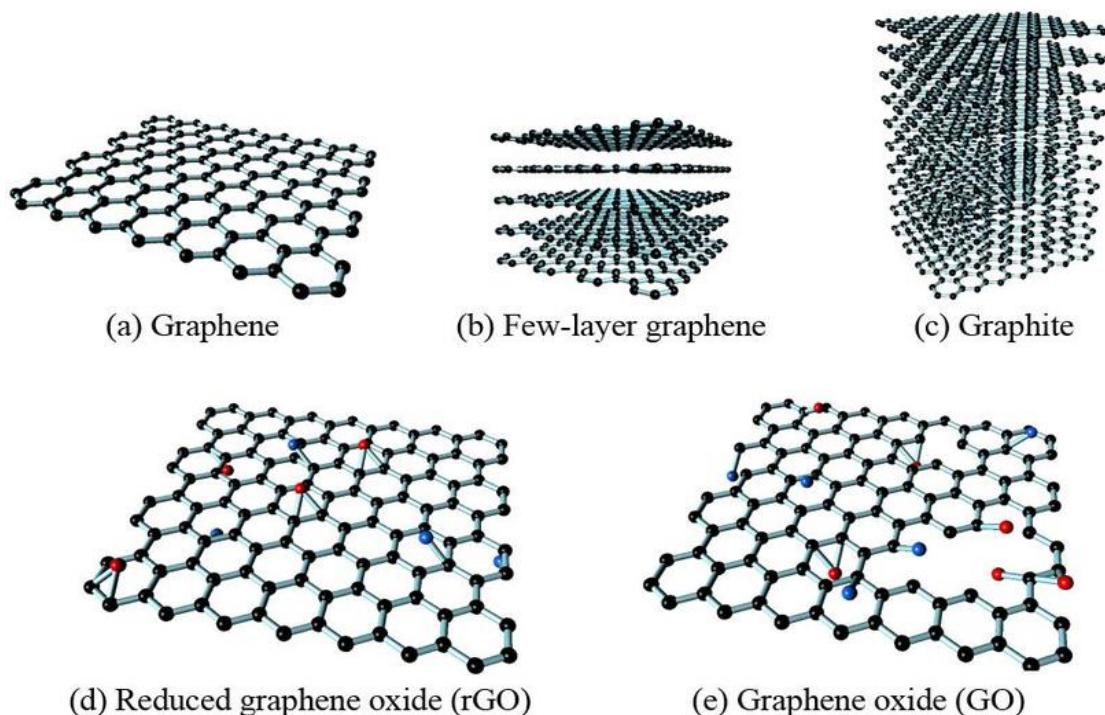


Figure 1.4 - Some members of the graphene family: (a) graphene, (b) few-layer graphene, (c) graphite, (d) reduced graphene oxide (rGO), (e) graphene oxide (GO) [54].

Recently, due to their excellent adsorption capacity, magnetic graphene-based nanocomposite, have been explored as suitable material for the removal and recovery of metals from effluent solutions and waters [58]–[60]. Despite the wide range of magnetic materials, magnetite nanoparticles (Fe_3O_4) are becoming the top of interest due to their unique magnetic separation performances by simply applying an external magnetic field [59]–[61]. In addition, magnetic nanoparticles have several applications in water treatment and can be applied in other materials giving rise to particles-based composite adsorbents. These composites allowed rapid isolation from aqueous solutions for regeneration and recycling. The big advantage in using magnetic graphene-based nanocomposite is that they can reduce operating costs and time required for water or wastewater treatment [46], [62].

1.4. Objectives and outline of the thesis

In line with: (i) the high demand of TCE for high-tech applications, (ii) the associated issues of their production, and (iii) their emerging in water streams, as a consequence of their increasing use, the main goal of this research study is to contribute for the development of an efficient material to remove TCE from water, with potential for future application in the recovery of TCE from industrial areas or aquatic systems.

The specific objectives of this study are:

- To synthesise and characterize a magnetic graphene-based nanocomposite;
- To evaluate the efficiency of the nanocomposite to remove TCE, in particular, La, Eu and Tb, from aqueous solutions with low level of contamination (mimicking the values already found in some real systems);
- To evaluate the effect of pH and adsorbent dose on the removal efficiency;
- To study the efficiency of the nanocomposite to remove La, Eu and Tb from unary and ternary solutions;
- To model the kinetic and equilibrium data obtained using models described in the literature.

2. Experimental

2.1. Synthesis and characterization of magnetic graphene-based nanocomposite

The preparation of magnetic graphene-based nanocomposite (MG-bN) was carried out using a modification of the electrostatic self-assembly methodology proposed by Han et al. [63]. The overall electrostatic self-assembly consists in a total of three steps: the exfoliation of graphite, the synthesis of magnetite nanoparticles (Fe_3O_4 NPs) and further dispersion in 0.1 M HNO_3 to protonate their surface, and the third and last step consist in the electrostatic assembly of the surface positively charged of Fe_3O_4 NPs with the negatively charged flakes of exfoliated graphite (EG). For better understanding of the process, see Appendix A.

2.1.1. Exfoliation of graphite

The exfoliation of graphite was done by ultrasonic treatment (Sonics Vibra Cell Sonicator, VC70, 130 W, 20 kHz) in N,N-dimethylformamide (DMF). The function of DMF is to facilitate the exfoliation of the graphite by reducing the strength of the van der Waals attractions between the adjacent layers of graphite. Briefly, graphite powder (5 g, EDM 99.95 (in % C) Graphit Kropfuhl GmbH) was sonicated in DMF (100 mL, 99.50 % Carlo Erba) for 5 h, in a 250 mL volumetric glass beaker kept under ice bath (0-5 °C). For purification, the mixture was then centrifuged at 5000 rpm for 20 min. After centrifugation, filtration and drying under vacuum at room temperature, the EG was obtained as a powder.

2.1.2. Synthesis of magnetite nanoparticles

In this step, the magnetic nanoparticles were synthesized by oxidative hydrolysis of iron(II) in alkaline conditions according to the procedure described by Schwertmann and Cornell [64]. First, potassium hydroxide (1.899 g) and potassium nitrate (1.519 g) were dissolved in 25 mL of deoxygenated water (previously deoxygenated with N_2 under vigorous stirring for 2 h) in a three-necked volumetric flask (250 mL), kept under paraffin bath (60 °C) with mechanical stirring at 500 rpm, under N_2 atmosphere. Iron(II) was added as ferrous sulphate ($\text{FeSO}_4 \cdot 7\text{H}_2\text{O}$) (4.745 g) dissolved in 25 mL of deoxygenated water, and then was carefully added drop-by-drop to the alkaline solution and the stirring was increased to 700 rpm. The solution was then left to react for 30 min. After reaction, the solution was left

under N₂ atmosphere at 90 °C, without stirring for 4 h. For purification, the obtained dark powder was washed several times with deoxygenated water and then with ethanol (96 %). At the end, the powder was dried at 40 °C for solvent evaporation.

2.1.3. Preparation of the magnetic graphene-based nanocomposite

The last fabrication step of the MG-bN consisted in the electrostatic self-assembly of Fe₃O₄ NPs at the sheets of exfoliated graphite. In this step, exfoliated graphite (100 mg) was dispersed in 100 mL of Milli-Q water and then sonicated for 1 h (Sonics Vibra Cell Sonicator, VC70, 130 W, 20 kHz), for an additional exfoliation. At the same time, Fe₃O₄ NPs (100 mg) were dispersed in 100 mL of 0.1 M HNO₃ and kept for 1 h. Afterwards, the obtained positive surface charge Fe₃O₄ NPs were added to the EG dispersion under sonication for 1 h. Finally, the MG-bN was carefully recovered with a powerful magnet. The MG-bN was washed several times with ultra-pure water and then with ethanol (96 %). At the end, the powder was dried at 40 °C for solvent evaporation.

2.1.4. Characterization techniques

Fourier transform infrared (FTIR) spectra (KBr pellets) of the samples were obtained at resolution of 4 cm⁻¹ and recorded as transmittance from 4000 to 400 cm⁻¹ using a spectrometer Bruker TENSOR II.

The crystallite phase and structure determination of the samples were recorded using X-Ray diffractometer Philips X'Pert equipped with CuK α monochromatic radiation source (0.1541 nm, 40 kV and 45 mA) at room temperature. The Scherrer equation [65] was applied considering the Scherrer correction factor ($K = 0.9$).

Raman spectra were obtained using a combined Raman-AFM-SNOM confocal microscope (alpha 300 RAS+, WITec, Germany). Nd:YAG laser operating at 532 nm was used as excitation source. The power of the laser was varied from 0.1 to 1 mW, in order not to damage/heat the sample.

For scanning transmission electron microscopy (STEM) analysis, samples were prepared by evaporating dilute suspensions of the nanocomposite on a copper grid coated with an amorphous carbon film. Experiments were performed on a HR-FESEM SU-70 Hitachi instrument operating at 25 kV.

For determination of total iron content in the MG-bN, ca. 10 mg of nanocomposite was added to 10 mL of HCl (30 %, v/v) in a Teflon sealed vessel, for 2 h at 50-60 °C (VENTICELL MMM). The digested solution was then transferred to 50 mL vials and the volume was adjusted with Milli-Q water. For quality control replicate ($n = 3$) and blanks were carried out in the same digestion batch. The concentration of iron in the samples was then quantified by flame atomic absorption spectroscopy (Perkin Elmer, model AAnalyst 100), using a five-standards calibration curve (0, 1, 2, 3, 4, 5 ppm)¹¹.

Zeta potential experiments were conducted with a Malvern Zetasizer Nano ZS particle analyser (Malvern Instruments Ltd. Malvern). The electrokinetic measurements were taken by dispersing the samples (dispersions of 15 mg of nanocomposite mixed in a 0.01 M NaCl at different pH values ranging from 2 to 10) and transferred to a folded capillary zeta cell, and following the equipment instructions.

Magnetic measurements were performed using Quantum Design MPMS 3 SQUID-VSM. Field Cooled (FC) magnetic DC susceptibility measurements were done from 2 to 300 K with an applied field of 100 Oe¹². The magnetization measurements as function of the applied field were done at 4, 300 and 400 K.

2.2. Adsorption experiments

Adsorption is considered as one of the most cost-effective methods in water treatment, specially handling low concentration streams and meeting severe treatment levels [66]. Adsorption occurs when a gas or a liquid solute accumulates on the surface of a solid or a liquid (adsorbent), forming a molecular or atomic film (the adsorbate). The adsorbate can be fixed through physical or chemical bonds onto an adsorbent, and accordingly, physical or chemical adsorption will occur.

The synthesized magnetic nanocomposite was investigated as adsorbent for the uptake of La(III), Eu(III) and Tb(III) from water. The adsorption experiments carried out included the study of pH and amount of adsorbent, the kinetic and equilibrium in unary and ternary solutions. Well known models were then used to analyse the kinetic and equilibrium data

¹¹ These solutions were prepared pipetting 0, 100, 200, 300, 400 and 500 μ L, respectively, of the provided 1000 ppm iron standard solution into a 100 mL volumetric flask and dilute to the mark with 2 % nitric acid.

¹² Oersted (symbol Oe) is the unit of the auxiliary magnetic field H_c .

obtained. To better understand adsorption experiments set-up, see Appendix B- Adsorption experiments.

2.2.1. Reagents

All solutions were prepared with analytical range chemicals (AR grade) and ultra-pure Milli-Q water produced by a Millipore system. Certified commercial standards solutions of lanthanum, europium and terbium ($1002 \pm 1 \text{ mg L}^{-1}$), were purchased from SCP Science. Two solutions, 0.1 M NaOH and 0.01 M HNO₃, were prepared and used for pH adjustments.

2.2.2. Glassware cleaning procedures

All the glass material used in the experimental work was previously acid washed to avoid possible contaminations. It is important to make a prior and adequate washing of the material to be used, since the impact of solute losses can be very significant since the lanthanides concentrations in the samples to be analysed are low.

In the first place, all glassware was washed several times with tap and distillate water and then filled with nitric acid 25 % (v/v) for 24 h. Then, the material was rinsed again several times with tap, distillate and Milli-Q water. After cleaning procedures, the material was dried at room temperature.

During each experiment and sample collection, the syringes and sample vials used to collect the different aliquots were washed with 2 % nitric acid, followed by Milli-Q water and then a final wash with the lanthanide solution before collecting each sample.

2.2.3. The effect of pH on the adsorption of La(III), Eu(III) and Tb(III) by the magnetic graphene-based nanocomposite

The effect of pH on the adsorption of La(III), Eu(III) and Tb(III) by the MG-bN was studied for six different pH values, ranging from 2 to 10, and using ternary solutions with an initial concentration of 0.1 mg L^{-1} in each element. The solutions of NaOH and HNO₃, previously prepared, were used for pH adjustments. After pH stabilisation, 100 mL of each solution were transferred to SCHOTT flasks, and ca. 5 mg of MG-bN were added to each one. All experiments were done in duplicate. The samples were kept under agitation in an incubator shaker HWY-200D from Lan Technics, for 48 h. From each flask, five sample

aliquots for ICP-OES¹³ analysis were taken, at time zero (before MG-bN addition), and after 1, 3, 6, 24 and 48 h. The adsorbent was magnetically recovered. The ICP-OES analyses were carried out at the Laboratório Central de Análises (LCA-UA).

2.2.4. Kinetic experiments

To investigate the kinetics of the adsorption process, the time profile of La(III), Eu(III) and Tb(III), onto MG-bN was evaluated in unary and ternary solutions, and for two doses of adsorbent material (10 and 50 mg L⁻¹). For this purpose, batch experiments were carried out by adding the doses of adsorbent, accurately weighted, with a fixed volume of lanthanides solution (500 mL), in 1000 mL two-necked round bottom flask. The initial concentration of lanthanides was fixed in all assays and was 0.1 mg L⁻¹. For control, another solution with no adsorbent was also prepared (with this, it is possible to know if the absorption is only due to the MG-bN or if there are other agents influencing the results). The pH of these solutions was previously adjusted to 7.7 ± 0.1. The suspensions were mechanically stirred at room temperature and aliquots (ca. 10 mL) were collected at different times (0, 5, 10, 15, 20, 25, 30 and 45 min, and 1, 1.5, 2, 4, 6 and 24 h), then carefully acidified with HNO₃ 65 %, to pH < 2, and then analysed by ICP-OES at the LCA-UA. All kinetic experiments were carried out in duplicate. For the kinetic studies, the amount of La(III), Eu(III) and Tb(III) ions adsorbed onto the MG-bN at each time interval (q_A , mg g⁻¹) was determined using Equation (1) and plotted against time (t , h).

$$q_A = (C_{A0} - C_A) \times \frac{V}{W} \quad (1)$$

where q_A is the amount of lanthanides uptake at time t (mg g⁻¹), V is the volume of solution (L), C_{A0} (mg L⁻¹) is the initial concentration of lanthanides, C_A (mg L⁻¹) is the concentration of lanthanides at time t and W is the mass of the adsorbent material (g).

¹³ Inductively coupled plasma optical emission spectroscopy (ICP-OES) is a trace-level, elemental analysis technique that uses the emission spectra of a sample to identify, and quantify the elements that are present in the sample [107].

2.2.5. Equilibrium isotherms experiments

The experimental procedure to obtain the equilibrium data was simple and similar to the one previously described. Different doses of MG-bN adsorbent (5, 10, 15, 20, 30 and 50 mg L⁻¹) were placed in contact with the unary and ternary solutions containing La(III), Eu(III) and Tb(III) at pH 7.7 ± 0.1. The initial concentration of lanthanides was fixed in all assays and was 0.1 mg L⁻¹. The experiments were conducted at room temperature for a total period of 24 h. Calculations were performed using Equation (1) where $q_A = q_{A,e}$ and $C_A = C_{A,e}$.

2.3. Modelling

2.3.1. Kinetics modelling

The kinetics of La(III), Eu(III) and Tb(III) was investigated and the experimental results were interpreted by three the most used kinetic models: Lagergren or pseudo-first order equation, pseudo-second order equation and Elovich model.

2.3.1.1. Pseudo first-order model

The first order rate equation or Lagergren's kinetics equation has been widely used for the adsorption of an adsorbate from an aqueous solution and is described by the non-reversible Equation (2), where S represents the adsorption sites, M is the adsorbate and SM is the concentration of adsorbate bound to the sorbent [67], [68]:



It is important to realize that this kinetic equation rests on five assumptions:

- a) Sorption only occurs on localized sites and involves no interaction between the sorbed ions;
- b) The energy of adsorption is not dependent on surface coverage;
- c) Maximum adsorption corresponds to a saturated monolayer of adsorbates on the adsorbent surface;
- d) The concentration of M is considered to be constant;
- e) The adsorbate uptake on the sorbent is governed by a first-order rate equation.

Lagergren's original paper expressed the pseudo-first order rate equation in 1898 [68] and is described by Equation (3).

$$\frac{dq_A}{dt} = k_1(q_{A,e} - q_A) \quad (3)$$

$q_{A,e}$ and q_A (mg g^{-1}) are the adsorbed phase concentration at equilibrium and at time t , respectively, and k_1 (h^{-1}) is the rate constant of pseudo-first order adsorption.

2.3.1.2. Pseudo second-order model

The pseudo-second order model contrary to the previous model, can predict the system behaviour over the whole range of sorption and, is also based on the sorption capacity of the solid [69], [70]. Equation (4) represents the kinetics of adsorbate removal by the pseudo second order model [67].



Making the same assumptions for the pseudo-first order model, except the adsorbate uptake on the adsorbent is governed by a second-order rate equation, the kinetics rate law is described by Equation (5) [67], [71].

$$\frac{dq_A}{dt} = k_2(q_{A,e} - q_A)^2 \quad (5)$$

k_2 ($\text{g mg}^{-1} \text{h}^{-1}$) is the rate constant of pseudo-second order adsorption.

2.3.1.3. Elovich model [67], [72]

The kinetics of adsorbate removal described by Elovich model is shown in Equation (9).

The following assumptions are assumed by the model:

- Sorption only occurs on localized sites and there is interaction between the sorbed ions or molecules.
- The energy of adsorption increases linearly with the surface coverage according to Equation (6).

$$Ea = Ea_0 + RT\beta q_A \quad (6)$$

where Ea is the activation energy (J) for the reaction, R ($\text{J mol}^{-1} \text{K}^{-1}$) is the ideal gas constant, T is the temperature (K), β is a constant proportional to the liquid molar volume and q_A is the adsorbate concentration at instant t (mg g^{-1}).

Then, the adsorption rate constant k_{ad} can be written by the Arrhenius equation:

$$k_{ad} = Cte \times \exp\left(-\frac{Ea}{RT}\right) = \alpha' \times \exp(-\beta q_A) \quad (7)$$

where α' is given by:

$$\alpha' = Cte \times \exp\left(-\frac{Ea_0}{RT}\right) \quad (8)$$

- c) The concentration of M is considered to be constant.
- d) The adsorbate uptake is negligible before the experiment (equivalent to an adsorbate uptake governed by a zero order rate equation).

Finally, the sorption rate can be written as:

$$\frac{dq_A}{dt} = \alpha \times \exp(-\beta q_A) \quad (9)$$

with $\alpha = C^y \alpha'$.

2.3.2. Equilibrium isotherm modelling

In adsorption studies, adsorption isotherms can provide some insight into the adsorption mechanism as well as the surface properties and adsorbent affinities. In summary, they indicate how molecules subjected to adsorption distribute themselves between fluid and solid phases at equilibrium. In this work, the most common adsorption equilibrium models- Langmuir and Freundlich models were used.

2.3.2.1. Langmuir isotherm

In 1916, Irving Langmuir published a new isotherm model for gases adsorbed to solids, which retained his name. This model is a semi-empirical isotherm derived from a proposed kinetic mechanism. The Langmuir isotherm theory assumes monolayer coverage of adsorbate over a homogenous adsorbent surface [73].

The Langmuir isotherm model is based on four assumptions: 1) The adsorption occurs at definite localized sites on the surface, normally called active centers; 2) the adsorption surface is homogeneous, which means that each site is able to bind a single molecule of adsorbing species; 3) adsorbed molecules do not interact with each other; 4) adsorption presents a maximum ($q_{A,m}$) corresponding to the monolayer formation.

This isotherm can be obtained by equalizing the adsorption and desorption rates, and is represented by [74], [75]:

$$q_{A,e} = \frac{q_{A,m} K_{A,L} C_{A,e}}{1 + K_{A,L} C_{A,e}} \quad (10)$$

where $q_{A,e}$ (mg g⁻¹) is the adsorbate concentration on the particle, $C_{A,e}$ (mg L⁻¹) is the adsorbate concentration in solution, $K_{A,L}$ (L mg⁻¹) is the Langmuir equilibrium constant and $q_{A,m}$ (mg g⁻¹) is the maximum concentration of the adsorbed species when one complete monomolecular layer of coverage is achieved.

The Langmuir model can be extended to multicomponent system, where different components that can form complexes with the surface sites are present. Equation (11) shows the Langmuir equation for multicomponent adsorption, where is represented the binding of component A to a surface of type L [76], [77]:

$$q_{A,e} = \frac{q_{A,m} K_{A,L} C_{A,e}}{1 + \sum_i K_{i,L} C_{i,e}} \quad (11)$$

2.3.2.2. Freundlich isotherm

Freundlich isotherm is an empiric equation frequently used in correlating aqueous phase experimental data. This model does not assume that the material coverage must approach a constant value corresponding to one complete solute monomolecular layer as $C_{A,e}$ gets larger [74]. Equation (12) shows the Freundlich isotherm:

$$q_{A,e} = K_F C_{A,e}^{1/n} \quad (12)$$

where K_F (μg^{1-1/n} L^{1/n} g⁻¹) and n are the Freundlich constants related to adsorption of the metals and adsorption intensity, respectively. A value of n between 1 and 10 indicates favourable adsorption and is related to the non-linearity of the model [78], [79].

2.3.3. Fitting the models to the experimental data

All these models were tested to study the sorption of La(III), Eu(III) and Tb(III) on the MG-bN using programs coded in MATLAB [80]. The kinetic parameters were optimized using the Nelder-Mead method, applying the average absolute relative deviation (AARD), Equation (13), as objective function.

$$AARD = \frac{100}{n} \sum \frac{|q_{i,calc} - q_{i,exp}|}{q_{i,exp}} \quad (13)$$

Concerning the equilibrium equations, the Langmuir and Freundlich parameters were optimized using once again the the Nelder-Mead method, but the sum squares errors (SSE), Equation (14), was the adopted objective function.

$$\text{SSE} = \sum (q_{i,\text{calc}} - q_{i,\text{exp}})^2 \quad (14)$$

3. Results and discussion

3.1. Characterization of magnetic graphene-based nanocomposite

The morphology and structure of the MG-bN and its precursors (graphite, EG and Fe₃O₄ NPs) were analysed by Fourier Transform Infrared spectroscopy (FTIR), Raman spectroscopy, X-ray Diffraction (XRD), Scanning Transmission Electron Microscopy (STEM) and Zeta potential. Magnetic measurements were also performed for the magnetic nanocomposite.

3.1.1. Fourier transform infrared analysis

Fourier transform infrared spectroscopy is an extremely rapid, non-destructive, time saving method that can detect a range of functional groups and is sensitive to changes in molecular structure. Figure 3.1 illustrates the FTIR spectra of Fe₃O₄ NPs, graphite, EG and MG-bN. The Fe₃O₄ NPs spectrum (Figure 3.1 a)) shows well-defined bands in the range of 400 – 881 cm⁻¹. These bands have been assigned to vibrational modes of magnetite. The two intense peaks at about 589 and 656 cm⁻¹ are due to the stretching vibration mode associated to the metal oxygen absorption band (Fe-O bonds in the crystalline lattice of Fe₃O₄). The bands of O-H groups are also present at 3161 cm⁻¹ and 1646 cm⁻¹ probably due to external agents [81], [82]. In the FTIR spectra of graphite (Figure 3.1 b)), the absorption band at ~3475 cm⁻¹ is related to the O-H stretching vibration. In addition to the resonances of oxygen-containing functional groups, the stretching absorptions of C=C groups are also visible in the spectrum at ~1650 and 1584 cm⁻¹. Comparing FTIR spectra of graphite with EG (Figure 3.1 c)) there is no significant differences between them. The FTIR spectrum of the MG-bN (Figure 3.1 d)) shows all the peaks present in graphite and EG spectra, together with the vibration band of Fe-O bond at ~604 cm⁻¹ that confirms the presence of the magnetic phase in the nanocomposite.

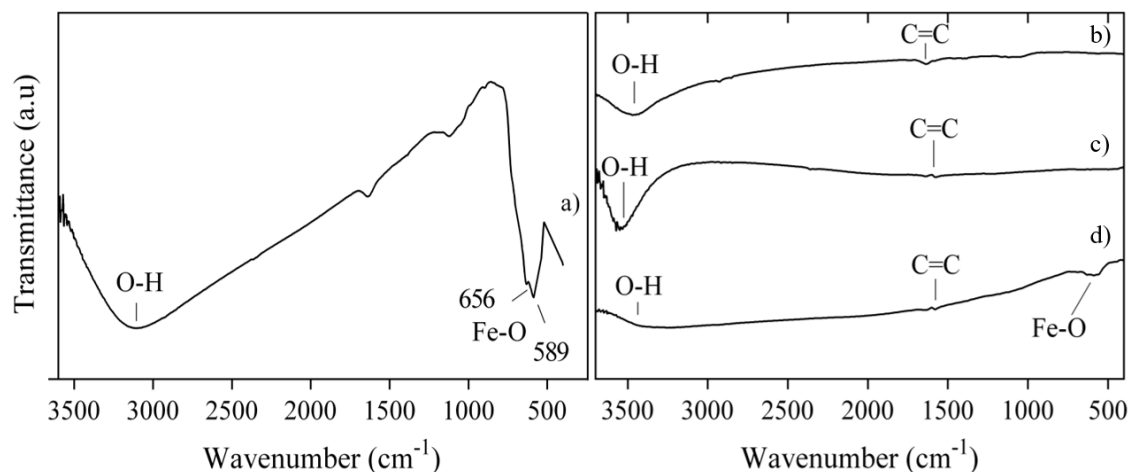


Figure 3.1 - FTIR spectra of a) Fe_3O_4 NPs, b) graphite, c) EG and d) MG-bN.

3.1.2. X-Ray diffraction analysis

X-Ray diffraction analysis is a very important technique that can disclose the crystal structure of solids, like lattice constants and geometry, identification of unknown materials, orientation of single crystals, defects and stresses [83]. In this work, XRD was made for structure determination of the samples (for comparison graphite diffractogram is also provided).

The diffraction pattern of EG (Figure 3.2 b)) gives a narrow peak (002) with very high intensity ($2\theta = 26.5^\circ$, corresponding to the interlayer distance $d = 0.34$ nm), characteristic of graphite (Figure 3.2 a)). Additionally, the broadened graphitic peak observed in EG suggests a decrease in the thickness of the samples in comparison to the precursor graphite (Figure 3.2 a)), confirming the exfoliation process [84]. According to the Scherrer equation, the EG are on average 17.2 nm in thickness while the average thickness of graphite flakes is 36 nm. In the diffractogram of Fe_3O_4 NPs (Figure 3.2 c)), the peaks at 2θ values of 18.19° , 30.00° , 35.39° , 36.99° , 43.06° , 53.43° , 56.98° and 62.54° can be assigned to (111), (220), (311), (222), (400), (422), (511) and (442) Bragg's reflections, respectively, and may be indexed on the face centred cubic structures of magnetite [85]–[87].

In the diffractogram of the magnetic nanocomposite (Figure 3.2 d)), the characteristic peaks of Fe_3O_4 and graphite remained unchanged, confirming that the deposition of the Fe_3O_4 NPs on the carbon substrate was successfully achieved.

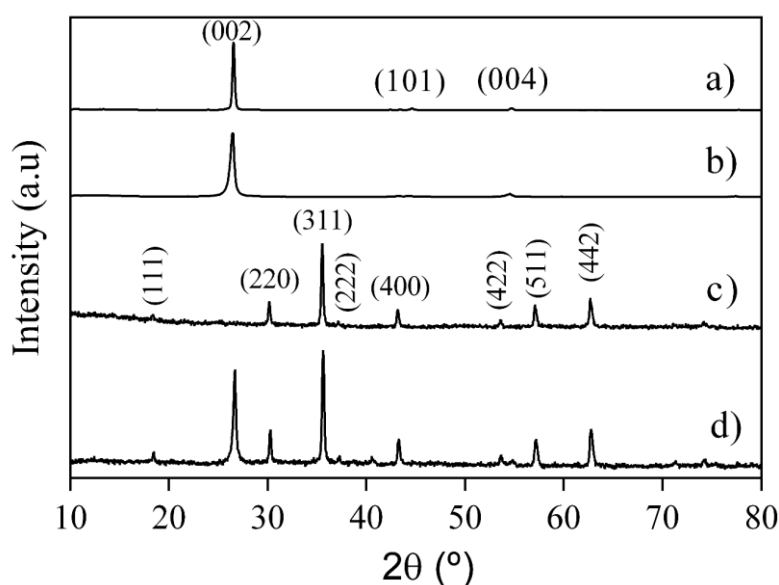


Figure 3.2 - XRD patterns of a) graphite, b) EG, c) Fe₃O₄ NPs and d) MG-bN. The characteristic peaks of the samples are marked.

3.1.3. Raman spectroscopy

Raman spectroscopy was applied to characterize the structural changes in the samples. This technique is strongly dependent upon electronic structure and thus, can be used in the study of carbon allotropes, including disorder and defect structures. Figure 3.3 shows Raman spectra of graphite, EG, Fe₃O₄ NPs and MG-bN.

The Raman spectra of graphite, EG and MG-bN exhibit simple structures characterized by two main bands (G- and 2D-bands, the Raman signature of graphitic sp² materials) in graphite and a third band in the EG and MG-bN ascribed to the D mode (~1344 cm⁻¹) that is induced by structural disorder (in this case defects and impurities in the carbon lattice, introduced during the ultrasonic treatment and/or Fe₃O₄ NPs deposition). The sharp and intense band that appears at around 1580 cm⁻¹ in all spectra (except Fe₃O₄ spectrum) is the G band that corresponds to the first-order scattering of the E_{2g} mode of the sp² carbon atoms in a 2D hexagonal lattice [88]. Since this band arises from the stretching of the C-C bond in graphitic materials, it is common to all sp² carbon systems.

Another band that appears in the Raman spectra of all kinds of sp² carbon materials, usually between 2500 and 2800 cm⁻¹, is the 2D band, and results from a second-order two-phonon process. The 2D mode is usually related to the crystalline structure and the stacking order, and also to the number of layers of graphene [89], [90].

The spectra of the nanocomposite were collected at 532 nm excitation laser wavelength with a lower laser power (0.1 mW) (Figure 3.3 d)). The choice of laser power is vital for collecting magnetite Raman spectra as phase changes are easily induced by the excitation laser. The spectrum preserves the signature of graphitic sp^2 materials (G and 2D bands), together with the D band associated with structural defects in the carbon lattice, and a peak at 660 cm^{-1} ascribed to magnetite nanoparticles.

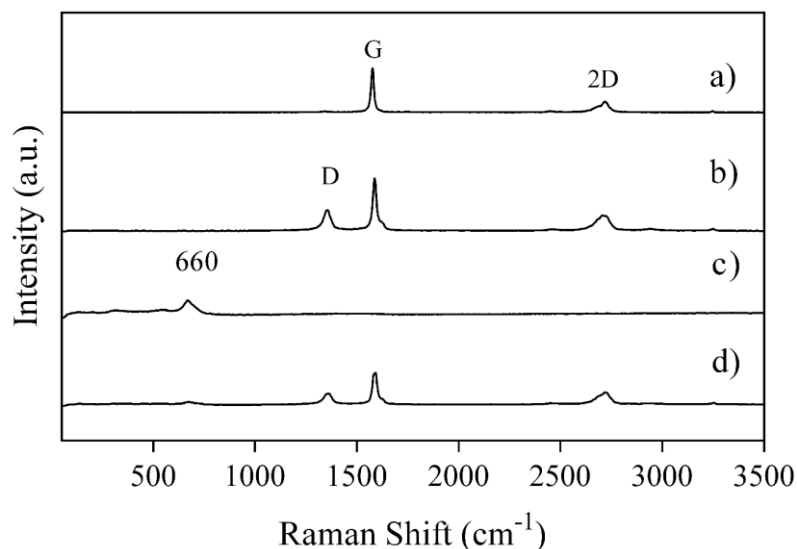


Figure 3.3 - Raman spectrum of a) graphite, b) EG, c) Fe_3O_4 NPs and d) MG-bN, showing the main Raman features, the D, G and 2D bands taken with a 532 nm excitation laser wavelength (1.0 or 0.1 mW).

3.1.4. Scanning transmission electron microscopy

STEM pictures were undertaken to characterize the morphologies of the commercial graphite, the EG, Fe_3O_4 NPs and the MG-bN. Figure 3.4 (a) and (b) show the TEM and SEM images of the as-received graphite powder material. It consists of a flake-like with smooth or jagged edges of different sizes ($\leq 45\text{ nm}$ Figure 3.4 (c) and (d) corresponds to the TEM and SEM images of EG, where it is clearly visible that the morphology and layer thickness of graphite sheets were completely changed after exfoliation. As it is visible in Figure 3.4 (e) and (f) Fe_3O_4 NPs were successfully synthesized, have spherical shape, display particle size below to 100 nm, and are aggregated into large particles. Figure 3.4 (g) and (h) show respectively, TEM and SEM images of the MG-bN. In the nanocomposite, Fe_3O_4 NPs are deposited on EG sheets as aggregates and not as single particles. In the TEM image, Fe_3O_4 NPs appear as dark dots with a diameter $< 100\text{ nm}$, on a lighter shaded substrate

corresponding to the EG. STEM images confirm the deposition of Fe_3O_4 NPs on EG and that the morphology of the nanoparticles is not affected by the presence of the carbon substrate.

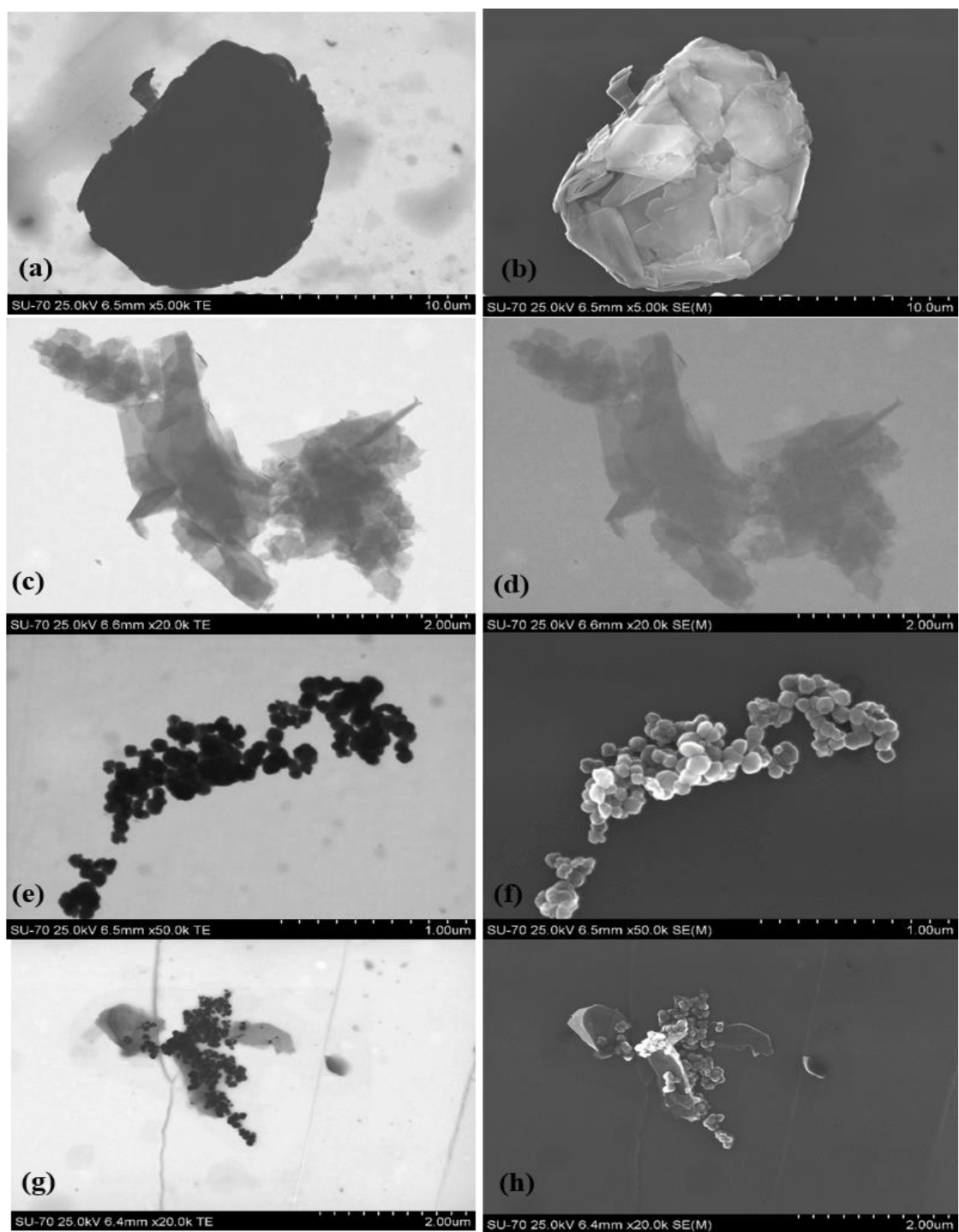


Figure 3.4 - TEM (left) and SEM (right) images of graphite (a and b), EG (c and d), Fe_3O_4 NPs (e and f) and MG-bN (g and h).

3.1.5. Atomic absorption spectroscopy

Atomic absorption spectroscopy was used to determine the total iron in the magnetic nanocomposite, after its total dissolution in an acid solution. The iron quantification was done using the calibration curve method (Figure 3.5).

The total Fe content in the nanocomposite is 32 %, which corresponds (by stoichiometric way) to a content in Fe_3O_4 of ca. 44 %.

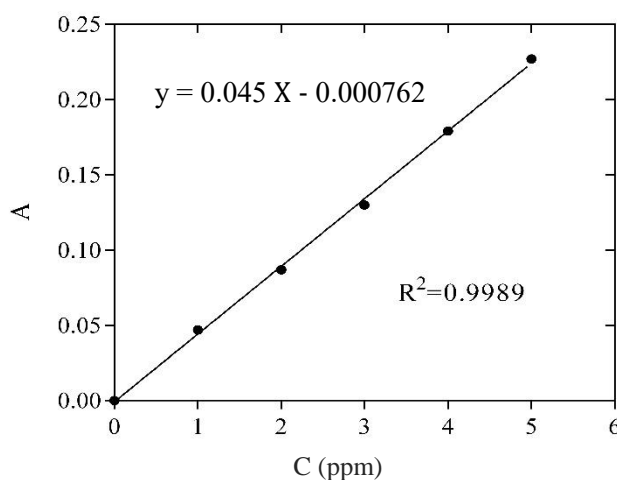


Figure 3.5 - Calibration curve for AAS with 5 different iron standard solutions (0, 1, 2, 3, 4, 5 ppm).

3.1.6. Zeta Potential

Zeta Potential was used to study the effective charge on the particles. This method is related to the electrostatic repulsion between them, thus it is extremely relevant to the practical study and control of adsorbents. Figure 3.6 shows the zeta potential as function of pH for a dispersion of MG-bN in NaCl solutions.

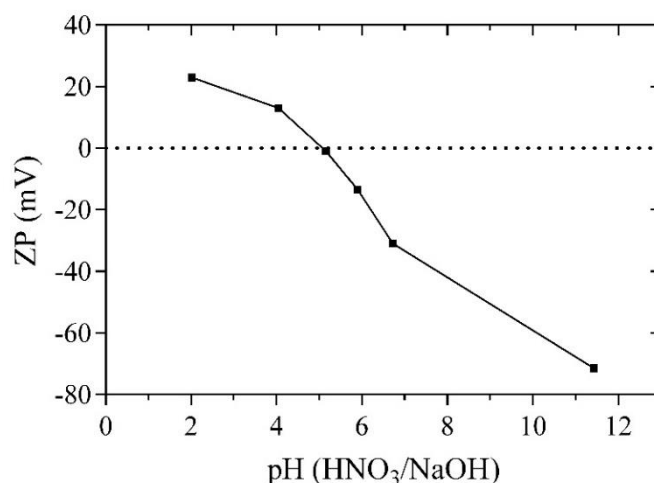


Figure 3.6 - Zeta potential of MG-bN powders in NaCl aqueous solution at different pH values.

The results indicate that the nanocomposite has zero charge at pH 5.2. This means that for pH values lower than 5.2 the surface of the MG-bN is positive, and as the solution pH is higher than 5.20 the materials surface acquires negative charge when the solution pH.

3.1.7. Magnetic measurements

Magnetic measurements were performed for the magnetic nanocomposite. As it can be seen from observation of Figure 3.7, the sample magnetization presents a fast approach to saturation in the presence of an external magnetic field (reaching saturation for about 5 k Oe) independently of the sample temperature. The MG-bN estimated saturation magnetization for 300 K is about 45 emu g⁻¹ nanocomposite and 102 emu g⁻¹ Fe₃O₄, which is in the same order of the saturation value of 92 emu g⁻¹ of bulk magnetite at room temperature [91]–[93]. The coercive fields (H_c) of MG-bN at room temperature is 90 Oe, which is low magnetic field (adequate to magnetic nanoparticles applications) and evidence the ferrimagnetic behaviour characteristic of magnetite nanoparticles with the reported sizes [94].

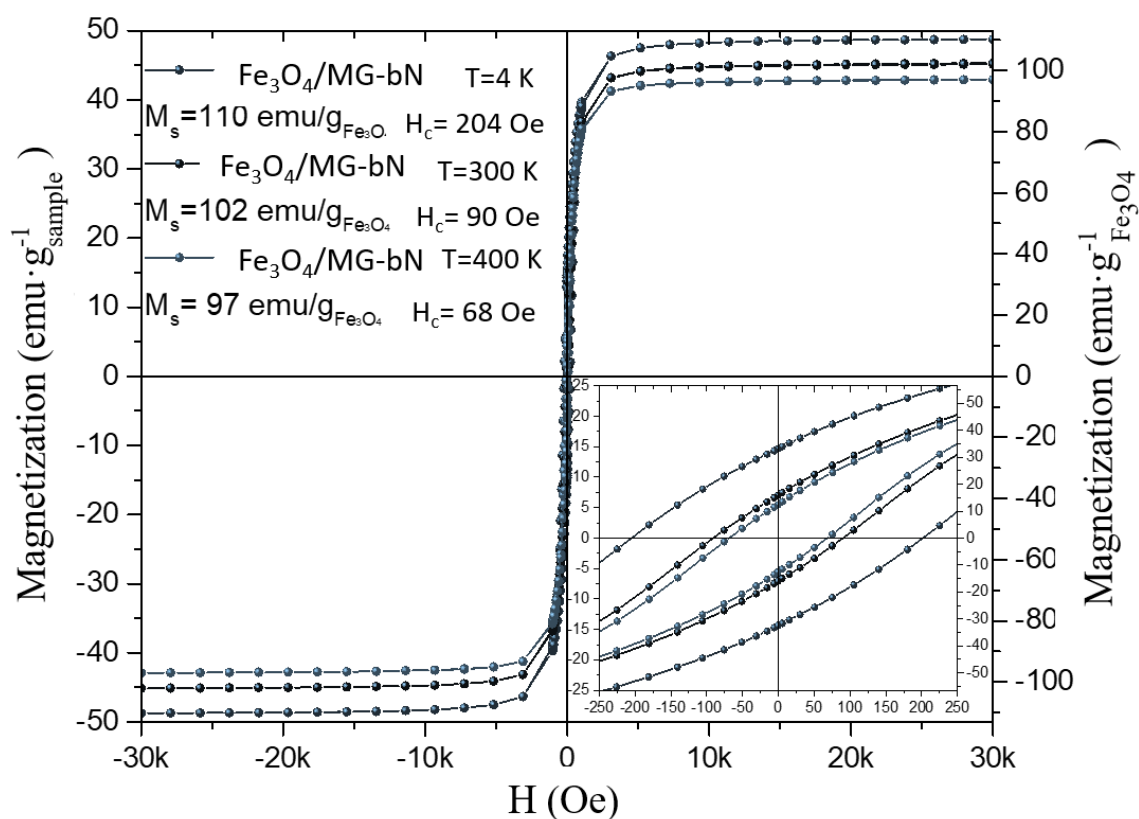


Figure 3.7 - Magnetization curves as a function of magnetic field for MG-bN. The right axis considers the estimated mass percentage of Fe_3O_4 which was determined using the Fe mass, and assuming that all magnetite is in perfect stoichiometry.

3.2. Adsorption of La(III), Eu(III) and Tb(III) by the magnetic graphene-based nanocomposite

3.2.1. Effect of pH

The solution pH is one of the most important variables affecting the adsorption process at solution-adsorbent interfaces. The influence of initial pH on the removal of lanthanides (ternary solution of La(III), Eu(III) and Tb(III)), through adsorption onto magnetic MG-bN was investigated over a pH range of 2-10. The initial lanthanides and MG-bN concentrations were 0.1 and 50 mg L^{-1} , respectively.

Figure 3.8 demonstrates how the removal of La(III), Eu(III) and Tb(III) by the MG-bN is highly affected by the pH of the surrounding environment. The adsorption efficiency (removal, %) was calculated using Equation (15), where C_{A0} is the initial concentration and C_{Ae} the remaining concentration of La(III), Eu(III) and Tb(III) in solution after the adsorption process.

$$\text{Removal} = \frac{C_{A0} - C_{Ae}}{C_{A0}} \times 100 \quad (15)$$

The results obtained allow us to conclude that the adsorption process of La(III), Eu(III) and Tb(III) onto the MG-bN is strongly pH dependent: a notorious increase on the removal efficiency from 0 % up to 95 % was observed by increasing the solution pH from 2 to 10. Moreover, small variations in the pH region of ca. 6 – 8 leads to a significant change in the removal efficiency, suggesting that the main mechanism involved in the removal of La(III), Eu(III) and Tb(III) by the MG-bN is based on electrostatic interactions. For example, the uptake of Eu(III) at pH 5.8 is 21.7 % and at pH 6 the removal increased to 30 %. At pH < 5, the surface of MG-bN is positively charged (see Figure 3.6) and the dominate species of La(III), Eu(III) and Tb(III) are the trivalent lanthanides ions (La^{3+} , Eu^{3+} and Tb^{3+} , respectively) [95]. As the solution pH increases, the number of negatively charged sites, at MG-bN surface also increases favouring the adsorption of cationic lanthanides due to electrostatic attraction. As a result, $\text{La}^{3+}/\text{La}(\text{OH})^{2+}$, $\text{Eu}^{3+}/\text{Eu}(\text{OH})^{2+}$, EuO^+ and $\text{Tb}^{3+}/\text{Tb}(\text{OH})^{2+}/\text{TbO}^+/\text{TbO}_2\text{H}(\text{aq})$, which are the dominant species of the lanthanides in study at pH 5 to 9 [95], may be adsorbed by MG-bN.

The highest removal efficiency was observed at pH 10. However, at this pH the magnetic separation (adsorbent-solution) was not efficient and some dark powder remained in the solution after the magnetic removal procedure, requiring another type of solid-liquid separation process (filtration or centrifugation). This clearly indicates that the magnetic nanocomposite loses part of its magnetic phase in very alkaline solutions (pH 10) and its application is not suitable for solutions with these pH values.

Although the removal of La(III), Eu(III) and Tb(III) by the MG-bN exhibits the same pattern vs. pH, it is notorious the similarity behaviour between europium and terbium. This can be explained by the fact that in the lanthanides group they are closer comparatively to lanthanum (and the closer they are, the greater is their behaviour similarity). In addition, the results from the pH study seem to point out that the MG-bN has more affinity¹⁴ to Eu(III) and Tb(III) comparing to La(III).

For the following experiments, pH 7.7 was chosen due to lanthanides speciation and to prevent the nanocomposite degradation.

¹⁴ The affinity of MG-bN was determined using equilibrium selectivity of the system, S_{12} , where 1 is La(III) and 2 is Eu(III) or Tb(III), and S is given by the ratio of the distribution coefficients (the concentrations values were expressed in molar units).

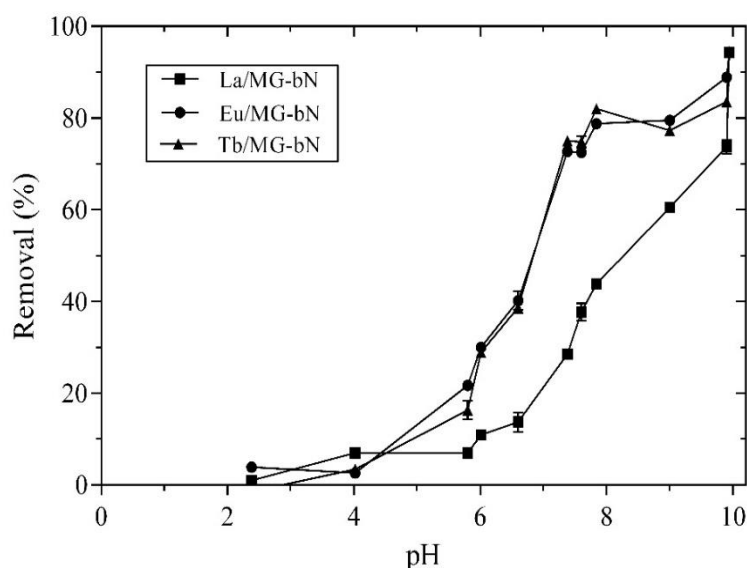


Figure 3.8 - Effect of pH on adsorption of La(III), Eu(III) and Tb(III) on MG-bN.

3.2.2. Kinetic studies

3.2.2.1. Effect of contact time and amount of adsorbent

The effect of contact time and amount of adsorbent on the removal of La(III), Eu(III) and Tb(III) from unary and ternary solutions was studied in the range of 0 to 24 h and for two concentrations of adsorbent (10 and 50 mg L⁻¹), at pH 7.7 ± 0.1, room temperature and an initial lanthanides concentration of 0.1 mg L⁻¹.

Unary solutions

Figure 3.9 displays the normalized concentration (C_A/C_{A0}) of each element in the liquid phase against time (plots a and b), for the two amounts of MG-bN used, and the removal percentage for the same experimental conditions (plots c and d). The open symbols correspond to the use of 50 mg L⁻¹ of MG-bN and the full symbols to the use of 10 mg L⁻¹. The dashed line represents the experimental data from the control assays. For clarity, and since the equilibrium was reached after one hour, the values are only presented until 4 h.

From the data on Figure 3.9, it is possible to conclude that in the presence of MG-bN, occurred a decrease on La(III), Eu(III) and Tb(III) concentrations in the liquid phase along time, and this decrease can only be related to the presence of the magnetic nanocomposite since in its absence, the lanthanides concentration in solution remained nearly constant (control). More, the decrease on La(III), Eu(III) and Tb(III) concentrations is fast at

beginning, then, for a short period of time, evolves into a slower kinetics until it reaches equilibrium. Such fact is explained by the large mass transport driving forces observed at beginning, since MG-bN is initially free of solutes.

It is important to realize that, when only 10 mg L^{-1} of MG-bN is used, the kinetic pattern and the efficiency of the removal process is similar for all elements, and no relevant differences between them were observed (i.e. error bars overlap). The low concentration of the elements under study, as well as the low mass of material used contribute to the variability of the results, not allowing to distinguish significant differences in the behaviour and affinity of the different lanthanides towards the magnetic nanocomposite. Under these experimental conditions, the MG-bN is able to remove ca. 30 – 40 % of La(III) or Eu(III) or Tb(III) after 1 h. However, if the amount of MG-bN used increases to 50 mg L^{-1} , not only the amount of lanthanides removed increases (ca. 20 % for La(III) and ca. 40 % for Eu(III) and Tb(III)) but also it can be noticed some differences on the kinetic behaviour of the different systems, something that did not happen for the lowest sorbent dose. For 50 mg L^{-1} of MG-bN ca. of 60 % of the La(III), 70 % of Eu(III) and 80 % of Tb(III) initially in solution can be removed from unary solutions. Additionally, equilibrium is also reached faster for higher MG-bN concentrations. In the case of the system La(III)/MG-bN the equilibrium is reached after a few minutes and for the Eu(III)/MG-bN and Tb(III)/MG-bN systems in less than an 1 h. To better understand the kinetic profile of the process, the pseudo-first order, the pseudo-second order and the Elovich models, were used to fit the kinetic curves, and the results will be presented and discussed in the next section.

Ternary solutions

An analogous study was performed for the lanthanides in ternary solutions (Figure 3.10). In general, the kinetic behaviour is similar for La(III), Eu(III) and Tb(III) single solutions; i.e. the removal is fast at the beginning and slows down when the equilibrium is attained, the equilibrium is achieved sooner and the removal percentages are higher for the highest mass of MG-bN. However, it is important to realize that in the ternary system and for a MG-bN concentration of 10 mg L^{-1} , it is visible a significant difference between the kinetic profile of La(III) and the ones of Eu(III) and Tb(III), which is not visible in the unary solution. Additionally, Figure 3.10 also shows that the equilibrium is achieved later in the ternary solution in comparison with the unary solutions, as well as the efficiency of removal is

smaller for all systems. This may be due to the free available adsorbent sites, and more cations in the medium competing for the same place.

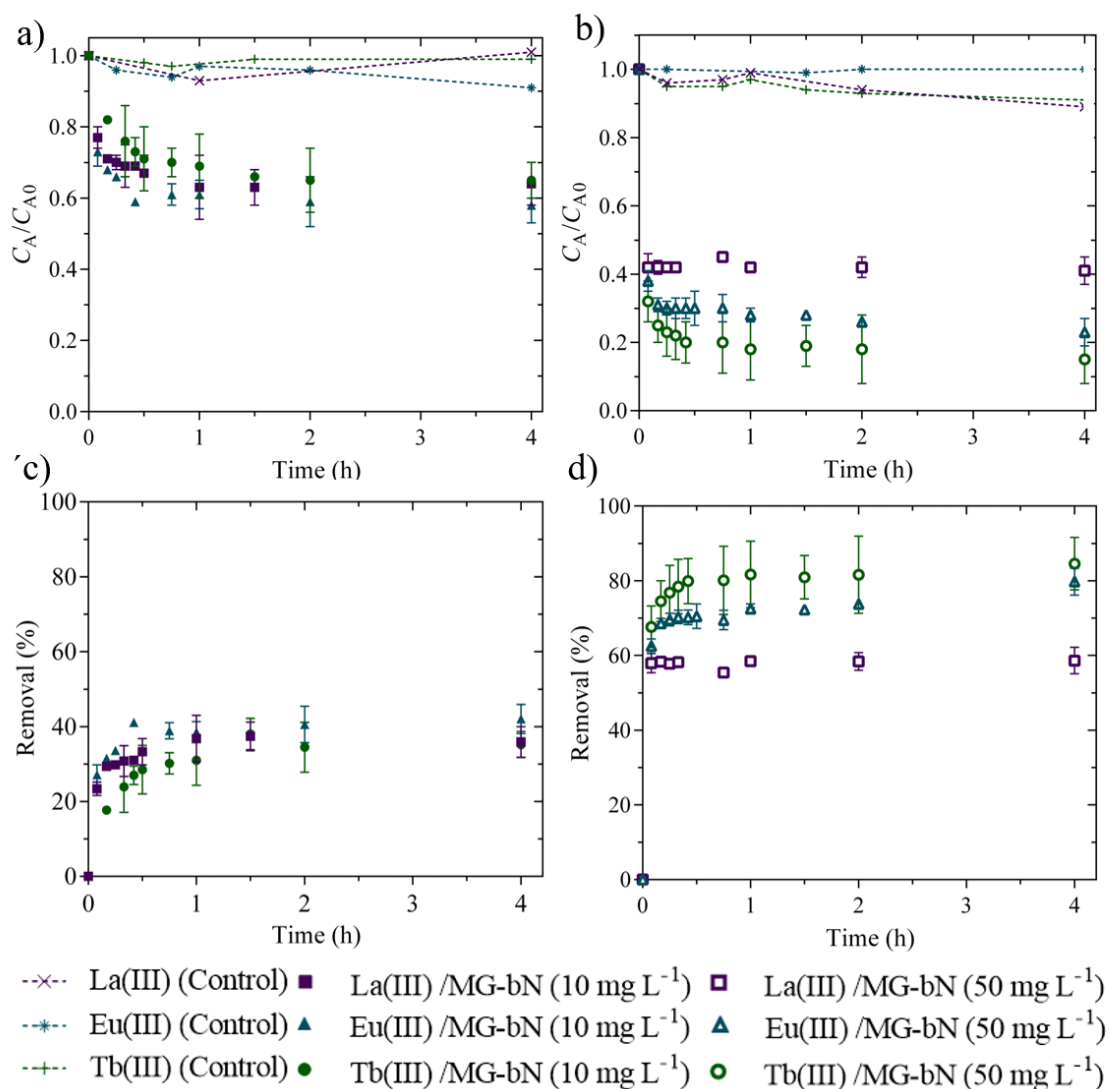


Figure 3.9 - Variation of normalized concentration and removal percentage of La(III), Eu(III) and Tb(III) from unary solutions (0.1 mg L⁻¹) with time, for different MG-bN concentrations. The bars represent the standard deviation. Experimental conditions: pH 7.7 ± 0.1, mechanical stirring speed 500 rpm, MG-bN dose 10 mg L⁻¹ (a and c) and 50 mg L⁻¹ (b and d).

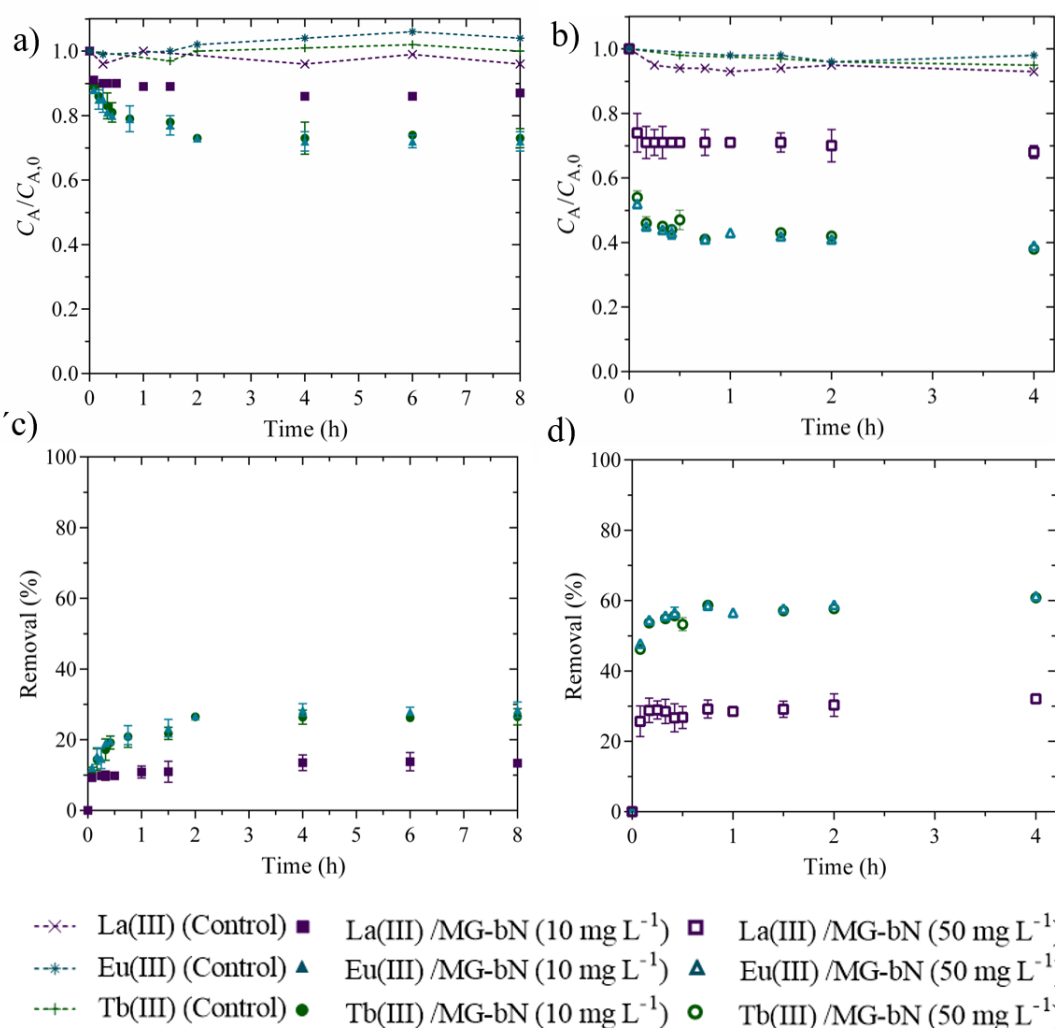


Figure 3.10 - Effect of contact time on the normalized concentration and removal percentage of La(III), Eu(III) and Tb(III) ternary solutions (0.1 mg L⁻¹) by MG-bN adsorbent. The bars represent the standard deviation. Experimental conditions: pH = 7.7 ± 0.1, mechanical stirring speed 500 rpm, MG-bN dose 10 mg L⁻¹ (a and c) and 50 mg L⁻¹ (b and d).¹.

3.2.2.2. Kinetics modelling

The experimental kinetic data of the removal of La(III), Eu(III) and Tb(III) by MG-bN, at room temperature for unary and ternary solutions, and using two different adsorbent doses (10 and 50 mg L⁻¹) were fitted by pseudo-first order, pseudo-second order and Elovich models, shown as Equations (3), (5), and (9).

Figure 3.11 and Figure 3.12, show the experimental (stars) and calculated (lines) concentrations of La(III), Eu(III) and Tb(III) in the magnetic nanocomposite along time, respectively for unary and ternary solutions. In unary solutions and, at low adsorbent dose (10 mg L⁻¹), equilibrium is reached after 1 h and the values of the experimental maximum

amount of La(III), Eu(III) and Tb(III) adsorbed are 3.84, 3.46 and 3.28 mg g⁻¹, respectively. For higher MG-bN concentration (50 mg L⁻¹), equilibrium is almost instantaneous and the values of the maximum amount of La(III), Eu(III) and Tb(III) adsorbed, decreased to 1.16, 1.36 and 1.21 mg g⁻¹, respectively.

For ternary systems, the uptake is lower compared to unary solutions, which was expected since there are more ions competing for the available sites on MG-bN, taking also more time to reach the equilibrium. At low adsorbent dose (10 mg L⁻¹), the values of the experimental maximum amount of La(III), Eu(III) and Tb(III) adsorbed are 1.22, 2.21 and 2.05 mg g⁻¹, respectively, while for higher MG-bN concentration (50 mg L⁻¹), the values of the maximum amount of La(III), Eu(III) and Tb(III) adsorbed, decreased to 0.650, 1.19 and 1.15 mg g⁻¹, respectively. These values show that La(III) as less affinity for the MG-bN than Eu(III) or Tb(III). The kinetic selectivities were also computing using Equation (16), where $q_{i,eq}$ and $C_{i,eq}$ are, respectively, the MG-bN concentration and the ions concentration at equilibrium and 1 and 2 designate La(III) and Eu(III) or Tb(III), respectively. The results have shown that Eu(III) and Tb(III) have higher affinity for the nanocomposite compared to La(III) - $S_{12} = 0.408$ (when 2 is Eu(III)) and $S_{12} = 0.471$ (when 2 is Tb(III)) using 10 mg L⁻¹ of MG-bN and $S_{12} = 0.298$ (when 2 is Eu(III)) and $S_{12} = 0.318$ (when 2 is Tb(III)) using 50 mg L⁻¹ of MG-bN.

$$S_{12} = \frac{\frac{q_{1,eq}}{C_{1,eq}}}{\frac{q_{2,eq}}{C_{2,eq}}} \quad (16)$$

In the whole, in the unary solutions the three used models, (pseudo-first order, pseudo-second order and Elovich models), satisfactorily describe the experimental data for all the studied adsorbent-adsorbate(s), with the large majority of the absolute average relative deviation (AARD) below 5 % and the correlation coefficients (R²) above 0.980 (Table 3.1). However, with only a few differences, the kinetics are better described by pseudo-second order model than by the pseudo-first order and Elovich models. These results are further supported by the comparison between the experimental q_{Ae} values, indicating that they are able to predict the kinetic behaviour of the lanthanides under study.

For ternary solutions, the experimental data are also better described by pseudo-second order and Elovich models, with an AARD < 4 % and R² > 0.990 (Table 3.2).

For all systems the kinetic constant, k_2 , of the pseudo-second order model also confirms that the removal process of La(III), Eu(III) and Tb(III) is faster for high doses of MG-bN.

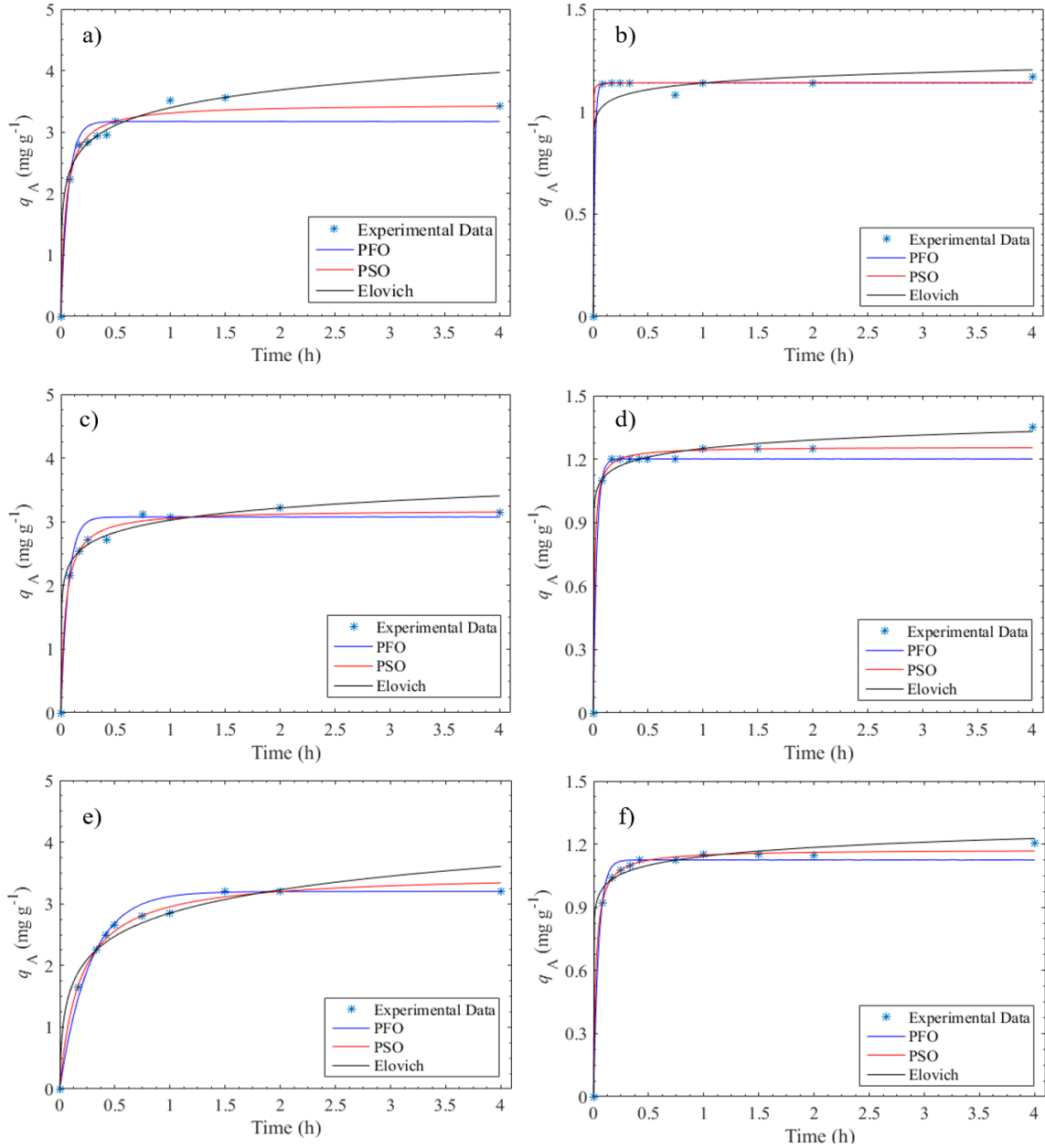


Figure 3.11 - Experimental and fitted data for: a) and b) La(III); c) and d) Eu (III); e) and f) Tb(III) using, respectively 10 and 50 mg L⁻¹ of MG-bN, unary solutions. Experimental conditions: pH 7.7 ± 0.1 and room temperature ca. 25 °C. For clarity, error bars for La(III), Eu(III) and Tb(III) are omitted.

Table 3.1 - Optimized kinetic parameters obtained from pseudo-first order, pseudo-second order and Elovich models at pH 7.7 ± 0.1 , unary solutions (0.1 mg L^{-1} with MG-bN concentration of 10 mg L^{-1} and 50 mg L^{-1} . For comparison, the experimental q_{Ae} is shown.

System	$q_{\text{Ae,experimental}}$ (mg g^{-1})	Pseudo 1 st -order model (10 mg L^{-1})				Pseudo 1 st -order model (50 mg L^{-1})				$q_{\text{Ae,experimental}}$ (mg g^{-1})
		k_1 (h^{-1})	q_{Ae} (mg g^{-1})	AARD (%)	R^2	k_1 (h^{-1})	q_{Ae} (mg g^{-1})	AARD (%)	R^2	
La(III)	3.42	15.05	3.17	5.65	0.974	67.95	1.14	0.904	0.998	1.15
Eu(III)	3.15	15.09	3.08	4.78	0.984	31.02	1.20	1.97	0.992	1.36
Tb(III)	3.22	3.68	3.20	2.90	0.994	21.27	1.13	2.21	0.994	1.21
System	$q_{\text{Ae,experimental}}$ (mg g^{-1})	Pseudo 2 nd -order model (10 mg L^{-1})				Pseudo 2 nd -order model (50 mg L^{-1})				$q_{\text{Ae,experimental}}$ (mg g^{-1})
		k_2 ($\text{g mg}^{-1} \text{ h}^{-1}$)	q_{Ae} (mg g^{-1})	AARD (%)	R^2	k_2 ($\text{g mg}^{-1} \text{ h}^{-1}$)	q_{Ae} (mg g^{-1})	AARD (%)	R^2	
La(III)	3.42	6.48	3.46	2.69	0.993	1.98×10^3	1.14	0.938	0.998	1.15
Eu(III)	3.15	7.38	3.18	1.90	0.997	69.73	1.26	1.56	0.995	1.36
Tb(III)	3.22	1.57	3.49	1.92	0.997	38.63	1.17	0.719	0.999	1.21
System	$q_{\text{Ae,experimental}}$ (mg g^{-1})	Elovich model (10 mg L^{-1})				Elovich model (50 mg L^{-1})				$q_{\text{Ae,experimental}}$ (mg g^{-1})
		α ($\text{mg g}^{-1} \text{ h}^{-1}$)	β (mg g^{-1})	AARD (%)	R^2	α ($\text{mg g}^{-1} \text{ h}^{-1}$)	β (mg g^{-1})	AARD (%)	R^2	
La(III)	3.42	1.55×10^3	2.42	3.51	0.984	2.31×10^9	21.62	4.15	0.989	1.15
Eu(III)	3.15	1.73×10^4	3.653	3.18	0.992	1.33×10^8	17.24	1.55	0.997	1.36
Tb(III)	3.22	1.00×10^2	1.829	4.77	0.983	7.74×10^6	16.33	2.06	0.996	1.21

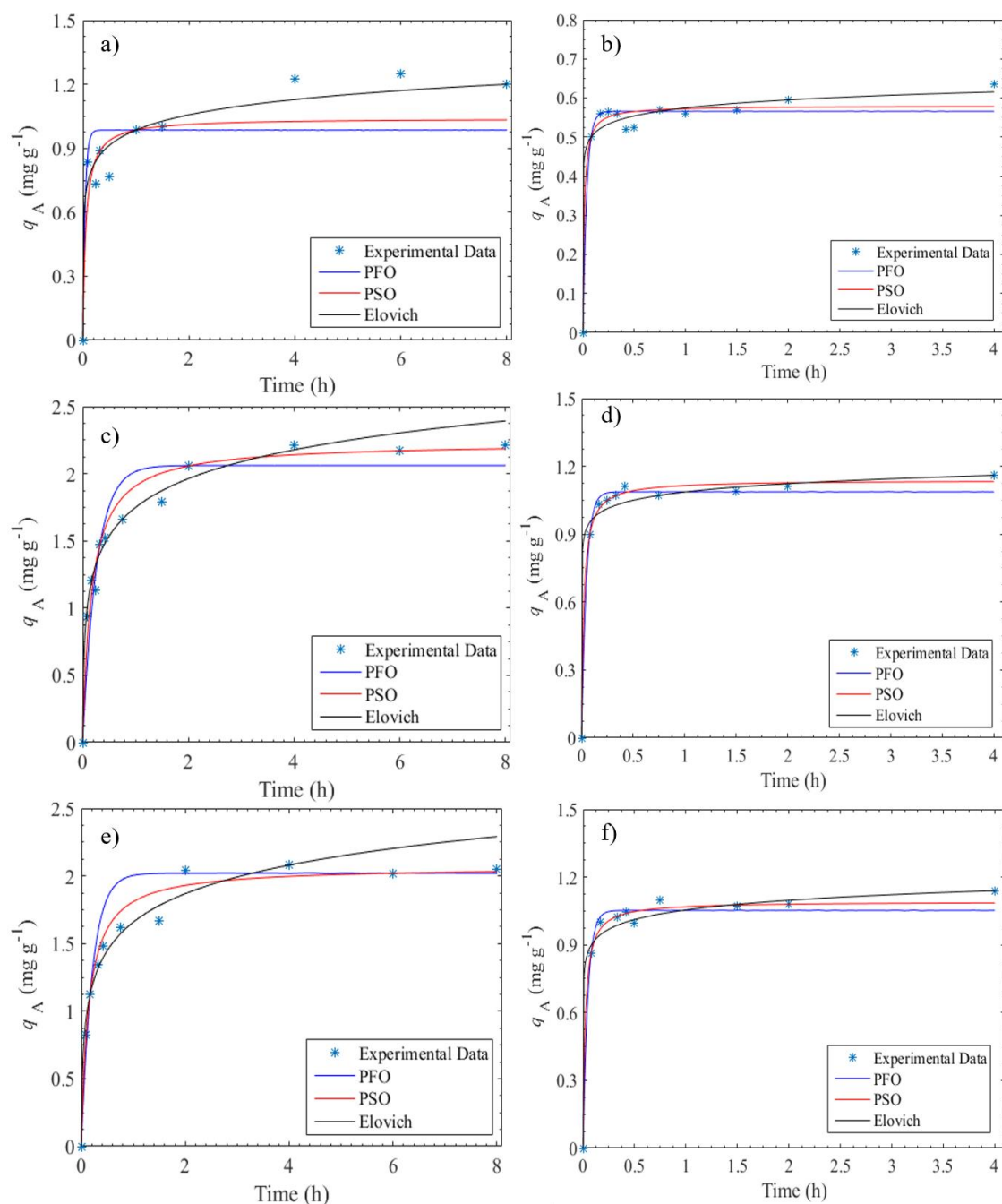


Figure 3.12 - Experimental and fitted data for: a) and b) La(III); c) and d) Eu (III); e) and f) Tb(III) using, respectively 10 and 50 mg L⁻¹ of MG-bN, ternary solutions. Experimental conditions: pH 7.7 ± 0.1 and room temperature ca. 25 °C. For clarity, error bars for La(III), Eu(III) and Tb(III) are omitted.

Table 3.2 - Optimized kinetic parameters obtained from pseudo-first order, pseudo-second order and Elovich models at pH 7.7 ± 0.1 , ternary solutions (0.1 mg L^{-1}) with MG-bN concentration of 10 mg L^{-1} and 50 mg L^{-1} . For better understanding, experimental q_{Ae} is also presented.

System	$q_{\text{Ae,experimental}}$ (mg g^{-1})	Pseudo 1 st -order model (10 mg L^{-1})				Pseudo 1 st -order model (50 mg L^{-1})				$q_{\text{Ae,experimental}}$ (mg g^{-1})
		k_1 (h^{-1})	q_{Ae} (mg g^{-1})	AARD (%)	R^2	k_1 (h^{-1})	q_{Ae} (mg g^{-1})	AARD (%)	R^2	
La(III)	1.22	23.50	0.985	13.34	0.87	26.90	0.566	2.99	0.984	0.650
Eu(III)	2.21	3.81	2.06	10.92	0.998	21.98	1.09	1.99	0.996	1.19
Tb(III)	2.05	4.79	2.02	9.79	0.963	21.57	1.05	2.78	0.992	1.15
System	$q_{\text{Ae,experimental}}$ (mg g^{-1})	Pseudo 2 nd -order model (10 mg L^{-1})				Pseudo 2 nd -order model (50 mg L^{-1})				$q_{\text{Ae,experimental}}$ (mg g^{-1})
		k_2 ($\text{g mg}^{-1} \text{ h}^{-1}$)	q_{Ae} (mg g^{-1})	AARD (%)	R^2	k_2 ($\text{g mg}^{-1} \text{ h}^{-1}$)	q_{Ae} (mg g^{-1})	AARD (%)	R^2	
La(III)	1.22	17.31	1.04	11.26	0.922	135.39	0.580	3.12	0.987	0.650
Eu(III)	2.21	2.65	2.23	6.59	0.997	41.33	1.14	1.45	0.998	1.19
Tb(III)	2.05	3.39	2.07	4.80	0.988	43.79	1.09	1.76	0.996	1.15
System	$q_{\text{Ae,experimental}}$ (mg g^{-1})	Elovich model (10 mg L^{-1})				Elovich model (50 mg L^{-1})				$q_{\text{Ae,experimental}}$ (mg g^{-1})
		α ($\text{mg g}^{-1} \text{ h}^{-1}$)	β (mg g^{-1})	AARD (%)	R^2	α ($\text{mg g}^{-1} \text{ h}^{-1}$)	β (mg g^{-1})	AARD (%)	R^2	
La(III)	1.22	1.44×10^3	9.68	6.63	0.974	8.58×10^6	33.92	2.99	0.991	0.650
Eu(III)	2.21	87.38	3.23	4.49	0.996	4.51×10^7	18.92	2.61	0.995	1.19
Tb(III)	2.05	70.22	3.28	5.12	0.984	1.74×10^6	16.27	2.73	0.995	1.15

3.2.3. Equilibrium studies and modelling

Figure 3.13 and Figure 3.14 show the equilibrium data together with the isotherms curves for the systems La(III)/MG-bN, Eu(III)/MG-bN, Tb(III)/MG-bN and La(III)/Eu(III)/Tb(III)/MG-bN, at constant operational parameters (pH, temperature, ionic strength and stirring speed). The Langmuir (Equation (10) for unary solutions and Equation (11) for multicomponent solutions) and Freundlich (Equation (12)) were the models chosen to fit the experimental data.

Unary solutions

Although the equilibrium data obtained for the unary systems show a high degree of dispersion and variability, it is possible to identify different tendency patterns between q_{Ae} and C_{Ae} for the different systems. While for Eu(III)/MG-bN and Tb(III)/MG-bN systems the isotherms display a favourable tendency, and the solid loading of these elements increases with concentration, under the range of tested conditions, without reaching a saturation *plateau*, for the system La(III)/MG-bN the isotherm has an unfavourable behaviour, with low adsorption at the low concentration region. A favourable isotherm means that its derivative decreases with increasing fluid concentration. Hence, at low concentration high solid loading can be achieved, leading to a high adsorption capacity at low concentrations in equilibrium [79].

Despite the great dispersion and variability of the experimental data, an attempt to fit the equilibrium data was made. In the range of experimental conditions used, the fittings of the theoretical models to the experimental data show high SSE and low R^2 values. In order to improve the equilibrium study, new isothermal assays were carried out but the results did not arrive in the predicted time and could not be considered in the current document. The estimated parameters of the equilibrium models studied, the coefficient of determination (R^2) and the sum of squared errors (SSE), are listed in Table 3.3, where K_L , q_{Ae} are Langmuir parameters and, K_F , and n are Freundlich parameters. For the system La(III)/MG-bN, only the Freundlich model can “fit” the equilibrium data ($R^2 = 0.963$, $SSE = 2.49$). The experimental data obtained for the Eu(III)/MG-bN and Tb(III)/MG-bN systems can be fitted with both Langmuir and Freundlich models with $SSE^* < 1.6$ and $R^2 > 0.909$. In all cases, the goodness of the fittings presented very high SSE values.

The adjusted value of the Freundlich's parameter n (Table 3.3) lower than 1 for La(III) and between 1 and 10 for Eu(III) and Tb(III) corroborate, respectively, the unfavourable and favourable nature of the adsorption process of these elements onto the MG-bN adsorbent (see Figure 3.13). Furthermore, the smaller K_F values obtained for La(III)/MG-bN indicate that this adsorbent has lower adsorption intensity and affinity for lanthanum [79], [96]. In contrast, the K_F values obtained for Eu(III)/MG-bN and Tb(III)/MG-bN systems are several orders of magnitude higher, and according to the Langmuir isotherm, the maximum adsorption of MG-bN toward Eu(III) and Tb(III) is 5.27 and 5.94 mg g⁻¹, respectively. Compared to other adsorbents (Table 3.4), the maximum MG-bN sorption capacity given by Langmuir isotherm is one of the highest, only surpassed by the synthetic analogue of heulandites [97].

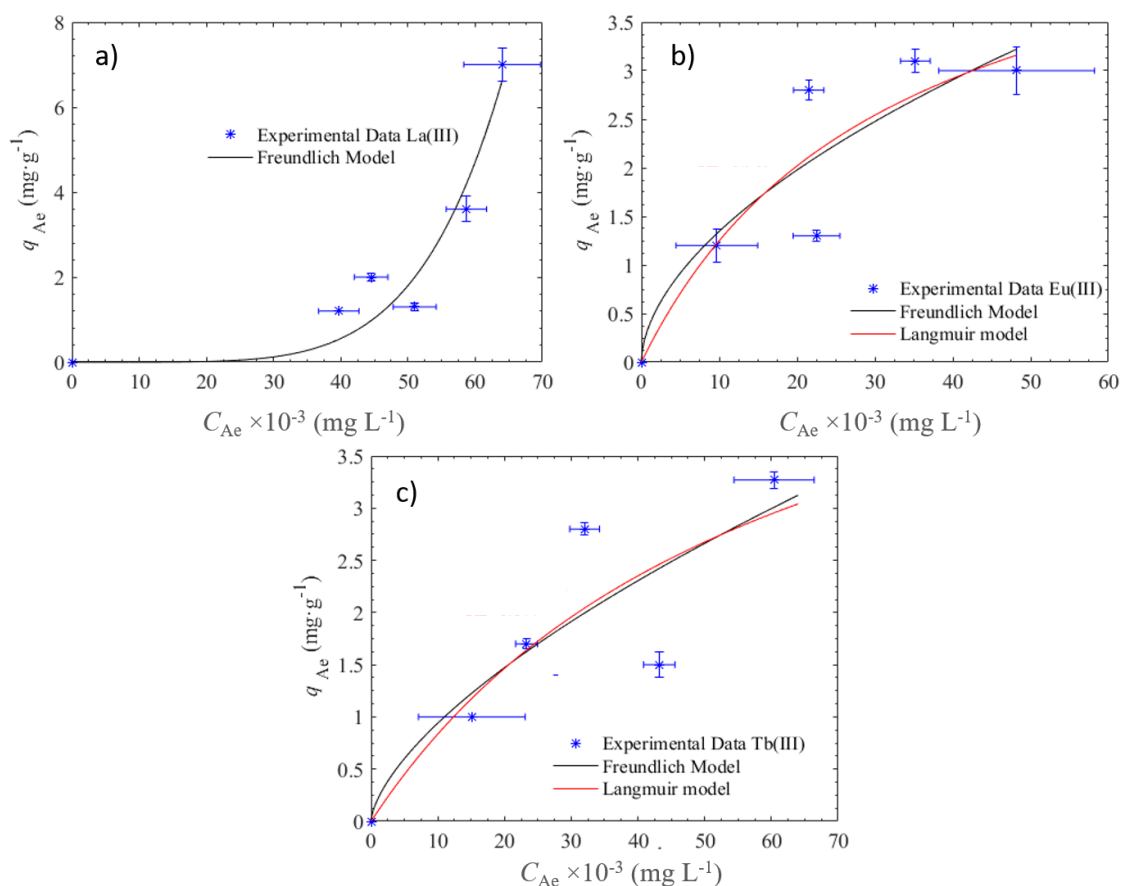


Figure 3.13 - Experimental data and unary isotherms modelling of a) La(III), b) Eu(III), c) Tb(III) unary solutions onto MG-bN (pH 7.7 ± 0.1 , initial concentration 0.1 mg L^{-1} and room temperature ca. 25°C). Error bars are also presented.

Table 3.3 - Modelling results of adsorption isotherms of La(III), Eu(III) and Tb(III) for unary Langmuir and Freundlich isotherms.

	Langmuir			
	K_L (L mg ⁻¹)	q_{Am} (mg g ⁻¹)	SSE	R^2
La				
Eu	31.1	5.27	1.38	0.909
Tb	16.4	5.94	1.63	0.877
	Freundlich			
	K_F (μg ^{1-1/n} L ^{1/n} g ⁻¹)	1/ n	SSE	R^2
La	1.99×10 ⁻⁹	5.26	2.49	0.963
Eu	0.375	0.556	1.43	0.905
Tb	0.212	0.645	1.62	0.878

Table 3.4 - Adsorption capacity for Eu(III) and Tb(III) of several materials used as sorbents in literature.

Adsorbent	Metal ion	q_{Am} (mg g ⁻¹)	q_{Am} (mmol g ⁻¹)	Reference
MG-bN	Eu(III)	5.27	0.0347	Present study
	Tb(III)	5.94	0.0374	Present study
ZSM-5 zeolite	Eu(III)		2.2 × 10 ⁻⁵	[98]
TiO ₂	Eu(III)		0.01	[99]
Synthetic analogue of heulandites	Eu(III)		0.1	[97]
Fe ₃ O ₄ @cyclodextrin composite (pH = 3.5)	Eu(III)		5.03 × 10 ⁻⁵	[100]
Fe ₃ O ₄ @cyclodextrin composite (pH = 5)	Eu(III)		8.35 × 10 ⁻⁵	[100]
P(HEMAHap)	Tb(III)		0.69 × 10 ⁻³	[101]
P(HEMA-Hap)phy	Tb(III)		0.31 × 10 ⁻³	[101]

Ternary solutions

Like for the unary solutions, the equilibrium data obtained for the ternary solutions also show a high degree of dispersion and variability, but, even so, it is possible to identify different tendency patterns between q_{Ae} and C_{Ae} for the different systems. Comparing Figure 3.13 and 3.14 it is possible to observe the similar behaviour of the lanthanides in ternary and unary solutions. The isotherm for the system La(III)/MG-bN is a convex, curved upward curve, meaning an unfavourable isotherm [96], [102]. For Eu(III)/MG-bN and Tb(III)/MG-bN systems the isotherms display a linear and/or favourable tendency, with an increase of the solid loadings with the concentration, under the range of tested conditions, without reaching a saturation plateau.

For the ternary solutions, the multicomponent Langmuir equation and the Freundlich model were chosen to fit the experimental equilibrium data. The estimated parameters of the equilibrium models adopted, the coefficient of determination (R^2) and sum of square error (SSE), are listed in Table 3.5. For the system La(III)/MG-bN, the fitting of the Freundlich model is poor ($R^2 = 0.555$, $SSE = 6.03$), while for the Eu(III)/MG-bN and Tb(III)/MG-bN systems both Langmuir and Freundlich models are able to fit data more accurately, with $SSE < 0.3$ and $R^2 > 0.952$. The optimized value of the Freundlich's parameter n (Table 3.5) higher than 1 for Tb(III) suggests favourable adsorption (represented by a concave, curved downward isotherm (Figure 3.14 c)) and equal to 1 for Eu(III) indicates a linear adsorption and, therefore, equal adsorption energies for all sites [96], [102].

Additionally, in ternary solutions, the Langmuir isotherm estimates a higher adsorption capacity of MG-bN towards Eu(III) and Tb(III), when compared to the unary solutions (Eu(III) ternary solutions shows an adsorption capacity of 23.66 mg g^{-1} and for unary solutions is only 5.27 mg g^{-1} , the same happens for Tb(III), 14.77 mg g^{-1} for ternary solutions and 5.94 mg g^{-1} for unary solutions).

Nevertheless, it must be highlighted that more points are needed to get a more accurately description of the equilibrium.

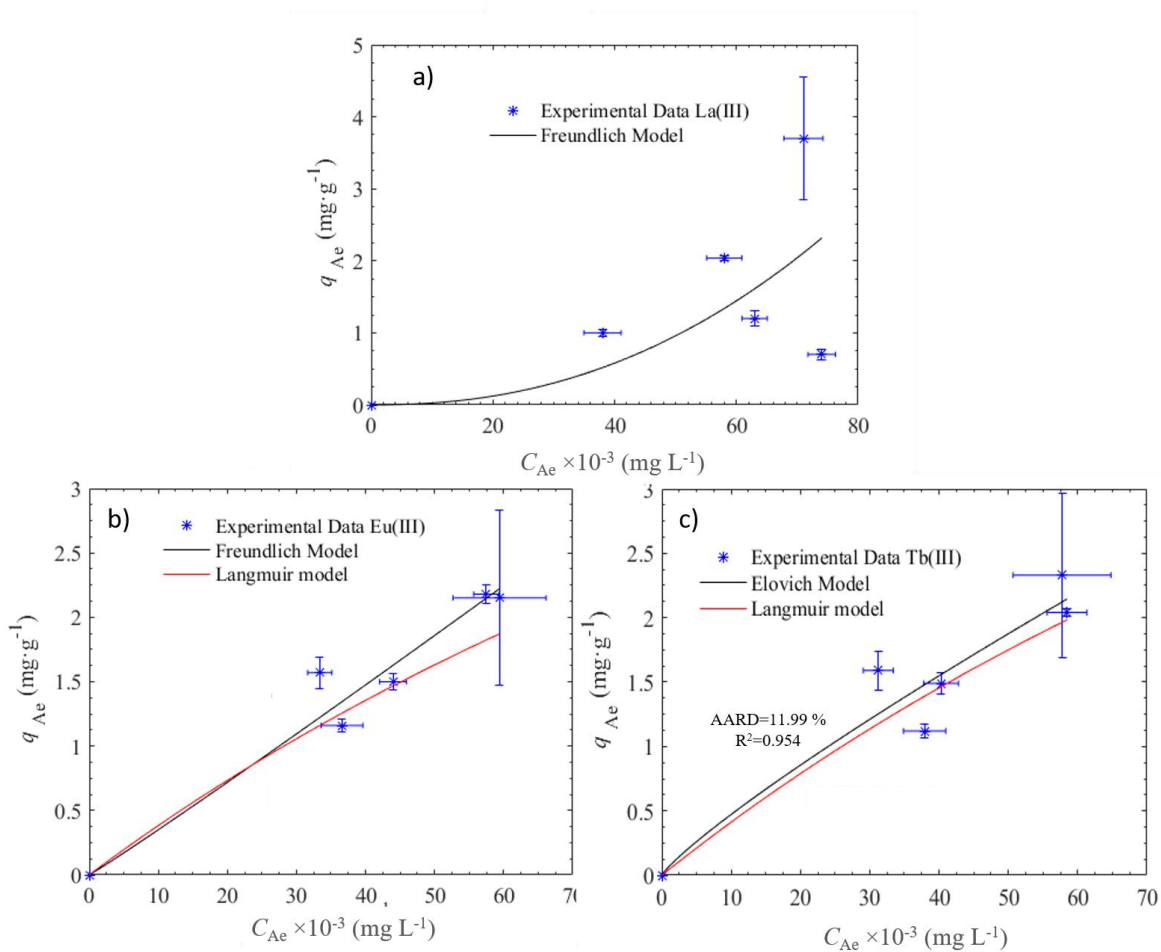


Figure 3.14 - Experimental data and multicomponent Langmuir isotherms and unary Freundlich isotherms for a) La(III), b) Eu(III), c) Tb(III) ternary solutions onto MG-bN (pH 7.7 ± 0.1 , initial concentration 0.1 mg L^{-1} and room temperature ca. 25°C). Error bars are also presented.

Table 3.5 - Modelling results of adsorption isotherms of La(III), Eu(III) and Tb(III) for multicomponent Langmuir isotherm and unary Freundlich isotherm.

	Langmuir			
	K_L (L mg ⁻¹)	q_{Am} (mg g ⁻¹)	SSE	R^2
La				
Eu	1.69	23.66	0.165	0.973
Tb	2.92	14.77	0.307	0.952
	Freundlich			
	K_F (µg ^{1-1/n} L ^{1/n} g ⁻¹)	1/ n	SSE	R^2
La	1.44×10 ⁻⁴	2.27	6.03	0.555
Eu	0.0322	1.04	0.165	0.973
Tb	0.0656	0.855	0.301	0.954

4. Conclusions and future work

The objective of this dissertation was to study the recovery of technological critical elements using a magnetic graphene-based nanocomposite. The magnetic nanocomposite was synthesized and characterized using different techniques, and then was studied as adsorbent for the uptake of lanthanum, europium and terbium cations, in non and competitive conditions. The kinetic and equilibrium results were interpreted by well-known and widely used models.

The magnetic nanocomposite was successfully prepared by a self-electrostatic approach using exfoliated graphite and magnetite nanoparticles as precursors. The characterization studies revealed that the synthesized material is composed by a mixture of graphene (less quantity), few layers graphene and graphite (major amount), with magnetite nanoparticles anchored on the surface of the carbon substrate.

The batch experiments performed revealed that MG-bN sorption efficiency toward La(III), Eu(III) and Tb(III) is strongly dependent on solution pH and concentration of MG-bN:

- The application of the magnetic nanocomposite to uptake La(III), Eu(III) and Tb(III) from aqueous solutions is limited to a pH range from 6 to 9. For pH values lower than 5, the MG-bN was totally inefficient uptaking lanthanides. However, as the pH starts to increase a huge increase of its efficiency is observed, and in the pH region 6 – 8 small differences on pH give rise to large differences in MG-bN efficiency. For pH values higher than 9, the nanocomposite loses part of its magnetic properties and its removal from solution using an external magnetic field loses efficiency. This pH dependency suggests that electrostatic interactions could be the main mechanism for the lanthanides uptake by the MG-bN.
- Only a few mg L^{-1} of MG-bN give rise to a significant decrease of lanthanides concentration in solution, but as expected, higher concentrations of MG-bN led to higher efficiency rates due to an increase on the available sorption sites.

The removal of La(III), Eu(III) and Tb(III) by the MG-bN is a fast process and in the optimized conditions the equilibrium could be reached in few minutes.

It is also notary that La(III) seems to have less affinity for the MG-bN when compared to Eu(III) and Tb(III). The isotherms obtained for the systems Eu(III)/MG-bN and Tb(III)/MG-

-bN are favourable while for La(III)/MG-bN is unfavourable. In general, the equilibrium models used to fit the experimental data show very high AARD values and low R^2 values, and obtaining further isotherms points are mandatory for a better description of the equilibrium. Nevertheless, the Langmuir adsorption capacity of MG-bN for Eu(III) and Tb(III) in unary solutions (5.3 and 5.9 mg g⁻¹, respectively) is higher than the ones found in literature for other adsorbents. When comparing the lanthanides unary solutions with ternary solutions, despite the high deviations, it is also noteworthy the increasing of the adsorption capacity.

The kinetics of lanthanides uptake is well described by the pseudo-second order model, which indicates that the process is of second order. Also, Elovich model achieved a good fit, with only a AARD < 4 % and $R^2 = 0.990$.

The operating conditions used to uptake lanthanides from diluted aqueous solutions using MG-bN are very attractive for application in various areas of environmental protection and lanthanide extraction, since do not require large amounts of sorbent, neither energy supply. In general, the proposed material and process prove to be a promising, effective and cost-effective method for the recovery of lanthanum, europium and terbium from diluted contaminated water streams.

As a suggestion for future work, it will be of interest to conduct regeneration studies by desorption methods. Also, a temperature study will be of interest to find out the real need to be monitored. Another relevant study would be to find out if magnetite nanoparticles and graphene-based material can work as adsorbents separately and future work must be focused on application of adsorbents on the recovery of lanthanides ions from real wastewater. Moreover, it will be interesting to accompany the batch experiments with column studies for better understanding the mechanism and the behaviour between the adsorbent and the elements of interest.

5. Publications and communications

It is worthy to mention that the research work developed under the scope of this master thesis was presented in national and international meetings and a paper is now under preparation.

Platform communication

- Lopes CB, Afonso EL, Pereira E, Vale C, Trindade T, Silva CM, 2017. *Recovery of rare-earth elements using a magnetic graphene-based nanocomposite*. I Reunião do Grupo de Carbono. 12-13 June, Porto, Portugal.

Panel communication

- Afonso EL, Pereira E, Trindade T, Silva CM, Lopes CB, 2017. *Synthesis and characterization of magnetic graphene-based nanocomposites for the recovery of rare-earth elements*. Materiais. 9-12 April, Aveiro, Portugal.

References

- [1] A. Cobelo-García, M. Filella, P. Croot, C. Frazzoli, G. Du Laing, N. Ospina-Alvarez, S. Rauch, P. Salaun, J. Schäfer, and S. Zimmermann, "COST action TD1407: network on technology-critical elements (NOTICE)-From environmental processes to human health threats," *Environ. Sci. Pollut. Res.*, vol. 22, no. 19, pp. 15188–15194, 2015.
- [2] M. Filella, "Fate of Technology-Critical Elements in the environment, with a focus on less-studied ones," in *18th International Conference on Heavy Metals in the Environment*, 2016, pp. 1–2.
- [3] The Geological Society, "Rare earth elements-A briefing note by the Geological Society of London," *The Geological Society*. London, p. 13, 2011.
- [4] N. G. Connelly, T. Damhus, R. M. Hartshorn, and A. T. Hutton, Eds., "Elements," in *Nomenclature of Inorganic Chemistry: IUPAC Recommendations 2005*, Cambridge: RSC Publishing, 2005, p. 366.
- [5] A. Tsamis and M. Coyne, "Recovery of Rare Earths from Electronic wastes: An opportunity for High-Tech SMEs," Brussels, Belgium, Nov. 2015.
- [6] N. Sui, K. Huang, C. Zhang, N. Wang, F. Wang, and H. Liu, "Light, middle, and heavy rare-earth group separation: A new approach via a liquid-liquid-liquid three-phase system," *Ind. Eng. Chem. Res.*, vol. 52, no. 17, pp. 5997–6008, 2013.
- [7] V. Zepf, "Rare Earth Elements: What and Where They Are," in *Rare Earth Elements. Springer Theses*, Berlin, Heidelberg: Springer, 2013, pp. 11–39.
- [8] W. C. Zhang, M. Rezaee, A. Bhagavatula, Y. G. Li, J. Groppo, and R. Honaker, "A Review of the Occurrence and Promising Recovery Methods of Rare Earth Elements from Coal and Coal By-Products," *Int. J. Coal Prep. Util.*, vol. 35, no. 6, pp. 295–330, 2015.
- [9] F. Wall, "Rare earth elements," in *Critical Metals Handbook*, First Edit., G. Gunn, Ed. Penryn, UK: John Wiley & Sons, Ltd., 2014, pp. 312–339.
- [10] K. T. Rim, "Trends in Occupational Toxicology of Rare Earth Elements," in *Rare Earth Elements in Human and Environmental Health: At the Crossroads between Toxicity and Safety*, G. Pagano, Ed. Singapore: Pan Stanford publishing Pte. Ltd, 2017, p. 256.
- [11] D. Kołodyńska and Z. Hubicki, "Investigation of Sorption and Separation of Lanthanides on the Ion Exchangers of Various Types," in *Ion Exchange technologies: Studies and Applications*, no. Iii, Kilislioglu A., Ed. InTech, 2012, pp. 101–154.
- [12] P. Koltun and A. Tharumarajah, "Life Cycle Impact of Rare Earth Elements," *ISRN Metall.*, vol. 2014, pp. 1–10, 2014.
- [13] G. A. Moldoveanu and V. G. Papangelakis, "Recovery of rare earth elements adsorbed on clay minerals: I. Desorption mechanism," *Hydrometallurgy*, vol. 117–118, pp. 71–78, 2012.
- [14] S. M. McLennan and S. Ross Taylor, "Geology, Geochemistry and Natural Abundances," *Encycl. Inorg. Bioinorg. Chem.*, 2012.
- [15] E. Anders and N. Grevesse, "Abundances of the elements: Meteoritic and solar," in *Geochimica et Cosmochimica Acta*, vol. 53, no. 1, 1989, pp. 197–214.

- [16] S. I. Levy, "The nature of the minerals and their mode of occurrence," in *The Rare Earths. Their Occurrence, Chemistry and Technology*, New York: Longmans, Green, and co., 1915, pp. 1–30.
- [17] F. Habashi, "Extractive metallurgy of rare earths," *Can. Metall. Q.*, vol. 52, no. 3, pp. 224–233, 2013.
- [18] C. K. K. Gupta and N. Krishnamurthy, "Resources of Rare Earths," in *Extractive metallurgy of rare earths*, vol. 37, no. 1, Boca Raton, London, New York, Washington, D.C.: CRC Press, 2005, pp. 71–146.
- [19] L. M. Suli, W. H. W. Ibrahim, B. A. Aziz, M. R. Deraman, and N. A. Ismail, "A review of rare earth mineral processing technology," *44th Annu. Meet. Can. Miner. Process. CIM, Ottawa*, vol. 79, no. 19, pp. 20–35, 2012.
- [20] A. H. King, R. G. Eggert, and K. A. Gschneidner, "The Rare Earths as Critical Materials," in *Handbook on the Physics and Chemistry of Rare Earths*, 1st ed., vol. 50, Elsevier B.V., 2016, pp. 19–46.
- [21] J. Gambogi, "Rare earths," *U.S. Geological Survey (USGS), Mineral Commodity Summaries, January 2016*, no. 703. USGS, pp. 134–135, 2017.
- [22] C. Sonich-Mullin, "Rare Earth Elements : A Review of Production , Processing , Recycling , and Associated Environmental Issues Rare Earth Elements : A Review of Production , Processing , Recycling , and Associated Environmental Issues," Cincinnati, OH, EPA 600/R-12/572, 2012.
- [23] N. Haque, A. Hughes, S. Lim, and C. Veron, "Rare Earth Elements: Overview of Mining, Mineralogy, Uses, Sustainability and Environmental Impact," *Rewiew*, vol. 3(4), no. 614–635, 2014.
- [24] K.-T. Rim, "Effects of Rare Earth Elements on the Environment and Human Health: A Literature Review," *Toxicol. Environ. Health Sci.*, vol. 8, pp. 189–200, 2016.
- [25] R. Earth, E. Review, and E. Risks, "Potential Human Health and Ecological Risks of Production , Processing , and Recycling of REEs," pp. 1–28.
- [26] The Editors of Encyclopædia Britannica, "Terbium (Tb)," *Encyclopaedia Britannica*, 2013. [Online]. Available: <https://www.britannica.com/science/terbium>. [Accessed: 01-Jan-2017].
- [27] E. Database, "Terbium," *Elements Database*, 2015. [Online]. Available: <http://www.elementsdatabase.com/Terbium-Tb-65-element/>. [Accessed: 24-Apr-2017].
- [28] F. Elbaz-Poulichet, C. Braungardt, E. Achterberg, N. Morley, D. Cossa, J. M. Beckers, P. Nomérage, A. Cruzado, and M. Leblanc, "Metal biogeochemistry in the Tinto-Odiel rivers (Southern Spain) and in the Gulf of Cadiz: A synthesis of the results of TOROS project," *Cont. Shelf Res.*, vol. 21, no. 18–19, pp. 1961–1973, 2001.
- [29] V. Funari, S. N. H. Bokhari, L. Vigliotti, T. Meisel, and R. Braga, "The rare earth elements in municipal solid waste incinerators ash and promising tools for their prospecting," *J. Hazard. Mater.*, vol. 301, pp. 471–479, 2016.
- [30] P. Sarojam, "Analysis of Wastewater for Metals using ICP-OES," *APPLICATION NOTE:ICP-Optical Emission Spectroscopy*. PerkinElmer, Inc., Shelton, p. 11, 2010.

- [31] R. S. Carvalho, A. L. Daniel-Da-Silva, and T. Trindade, "Uptake of Europium(III) from Water using Magnetite Nanoparticles," *Part. Part. Syst. Charact.*, vol. 33, no. 3, pp. 150–157, 2016.
- [32] Y. Sun, Q. Wang, C. Chen, X. Tan, and X. Wang, "Interaction between Eu(III) and Graphene Oxide Nanosheets Investigated by Batch and Extended X-ray Absorption Fine Structure Spectroscopy and by Modeling Techniques," *Environ. Sci. Technol.*, vol. 46, no. 11, pp. 6020–6027, 2012.
- [33] A. E. Gabor, C. M. Davidescu, A. Negrea, M. Ciopec, M. Butnariu, C. Ianasi, C. Muntean, and P. Negrea, "Lanthanum Separation from Aqueous Solutions Using Magnesium Silicate Functionalized with Tetrabutylammonium Dihydrogen Phosphate," *J. Chem. Eng. Data*, vol. 61, no. 1, pp. 535–542, 2016.
- [34] J. Ponou, G. Dodbiba, J. W. Anh, and T. Fujita, "Selective recovery of rare earth elements from aqueous solution obtained from coal power plant ash," *J. Environ. Chem. Eng.*, vol. 4, no. 4, pp. 3761–3766, 2016.
- [35] A. Earnshaw and N. N. Greenwood, "Scandium, Yttrium, Lanthanum and Actinium," in *Chemistry of the Elements*, Second., Butterworth-Heinemann, Ed. Leeds: Pergamon Press plc 1984, 1997, pp. 944–953.
- [36] The Editors of Encyclopaedia Britannica, "Lanthanum (La)," *Encyclopaedia Britannica*, 2012. [Online]. Available: <https://www.britannica.com/science/lanthanum>. [Accessed: 19-Feb-2017].
- [37] R. J. Moore, *Lanthanum: Compounds, Production and Applications*, 1st ed. New York: Nova Science Publishers, Inc., 2010.
- [38] A. Stwertka, "Europium," in *A guide to the elements*, 2nd ed., Oxford University press, 2002, p. 156.
- [39] J. Emsley, "Europium," *Royal Society of Chemistry*, 2012. [Online]. Available: <http://www.rsc.org/periodic-table/element/63/europium>. [Accessed: 22-Feb-2017].
- [40] The Editors of Encyclopaedia Britannica, "Europium (Eu)," *Encyclopaedia Britannica*, 2012. [Online]. Available: <https://www.britannica.com/science/europium>. [Accessed: 22-Feb-2017].
- [41] M. Winter, "Europium: the essentials," *The University of Sheffield and WebElements*, 2016. [Online]. Available: <https://www.webelements.com/europium/>. [Accessed: 27-Feb-2017].
- [42] C. R. Hammond, "Properties of the Elements and Inorganic Compounds," in *CRC Handbook of Chemistry and Physics, Internet Version 2005*, G. Baysinger, L. I. Berger, R. N. Goldeberg, H. V. Kehiaian, K. Kuchitsu, G. Rosenblatt, D. L. Roth, and D. Zwillinger, Eds. Boca Raton: CRC Press, 2005, pp. 702–845.
- [43] A. Stwertka, "Terbium," in *A guide to the elements*, 2nd ed., New York, Oxford: Oxford University press, 2002, p. 159.
- [44] Chemicool, "Terbium," *Chemicool Periodic Table*, 2012. [Online]. Available: <http://www.chemicool.com/elements/terbium.html>. [Accessed: 01-Mar-2017].
- [45] R. Khaydarov and O. Gapurova, "Application of carbon nanoparticles for water treatment," in *Water Treatment Technologies for the Removal of High-Toxicity*

- Pollutants*, M. Václavíková, K. Vitale, G. P. Gallios, and L. Ivaničová, Eds. Dordrecht: Springer, 2008, pp. 253–258.
- [46] D. K. Tiwari, J. Behari, and P. Sen, “Application of Nanoparticles in Waste Water Treatment,” *Carbon Nanotub.*, vol. 3, no. 3, pp. 417–433, 2008.
- [47] T. Pradeep and Anshup, “Noble metal nanoparticles for water purification: A critical review,” *Thin Solid Films*, vol. 517, no. 24, pp. 6441–6478, 2009.
- [48] M. Khajeh, S. Laurent, and K. Dastafkan, “Nanoadsorbents : Classification, Preparation, and Applications (with Emphasis on Aqueous Media),” *Chem. Rev.*, p. 41, 2013.
- [49] A. R. Tucker, “Review: New Sorbents for Solid-Phase Extraction for Metal Enrichment,” *CLEAN – Soil, Air, Water*, vol. 35, no. 6, pp. 548–557, 2007.
- [50] J. H. Deng, X. R. Zhang, G. M. Zeng, J. L. Gong, Q. Y. Niu, and J. Liang, “Simultaneous removal of Cd(II) and ionic dyes from aqueous solution using magnetic graphene oxide nanocomposite as an adsorbent,” *Chem. Eng. J.*, vol. 226, pp. 189–200, 2013.
- [51] G. Z. Kyzas, E. A. Deliyanni, and K. A. Matis, “Graphene oxide and its application as an adsorbent for wastewater treatment,” *J. Chem. Technol. Biotechnol.*, vol. 89, no. 2, pp. 196–205, 2014.
- [52] Y. Yao, S. Miao, S. Liu, L. P. Ma, H. Sun, and S. Wang, “Synthesis, characterization, and adsorption properties of magnetic Fe₃O₄@graphene nanocomposite,” *Chem. Eng. J.*, vol. 184, pp. 326–332, 2012.
- [53] M. Yusuf, F. M. Elfghi, S. A. Zaidi, E. C. Abdullah, and M. A. Khan, “Applications of graphene and its derivatives as an adsorbent for heavy metal and dye removal: a systematic and comprehensive overview,” *RSC Adv.*, vol. 5, no. 62, pp. 50392–50420, 2015.
- [54] S. F. Kiew, L. V. Kiew, H. B. Lee, T. Imae, and L. Y. Chung, “Assessing biocompatibility of graphene oxide-based nanocarriers: A review,” *J. Control. Release*, vol. 226, no. March, pp. 217–228, 2016.
- [55] Z. Singh, “Applications and toxicity of graphene family nanomaterials and their composites,” *Nanotechnology, Science Apl.*, vol. 2016:9, pp. 15–28, 2016.
- [56] O. Akhavan and E. Ghaderi, *Flash photo stimulation of human neural stem cells on graphene/TiO₂ heterojunction for differentiation into neurons.*, vol. 5, no. 207890. 2013.
- [57] M. Sharon and M. Charon, “Identification and characterization of graphene,” in *Graphene: An introduction to the fundamentals and industrial applications*, 1st ed., D. A. Tiwari, Ed. Massachusetts: Scrivener Publishing LLC, 2015, pp. 73–113.
- [58] N. Thi, V. Hoan, N. Thi, A. Thu, H. Van Duc, N. D. Cuong, D. Q. Khieu, and V. Vo, “Fe₃O₄ / Reduced Graphene Oxide Nanocomposite : Synthesis and Its Application for Toxic Metal Ion Removal,” vol. 2016, 2016.
- [59] J. Zhu, S. Wei, M. Chen, H. Gu, S. B. Rapole, S. Pallavkar, T. C. Ho, J. Hopper, and Z. Guo, “Magnetic nanocomposites for environmental remediation,” *Adv. Powder Technol.*, vol. 24, no. 2, pp. 459–467, 2013.

- [60] O. V. Kharissova, B. O. García, B. I. Kharisov, and U. O. Méndez, “Magnetic-Graphene-Based Nanocomposites and Respective Applications,” in *Advances in Carbon Nanostructures*, A. M. . Silva and A. C. Carabineiro, Eds. InTech, 2016.
- [61] L. Carlos, F. S. G. Einschlag, M. C. Gonzáles, and D. O. Mártire, “Applications of Magnetite Nanoparticles for Heavy Metal Removal from Wastewater,” in *Waste Water - Treatment Technologies and Recent Analytical Developments*, F. S. G. Einschlag and L. Carlos, Eds. InTech, 2013.
- [62] L. Ji, X. Bai, L. Zhou, H. Shi, W. Chen, and Z. Hua, “One-pot preparation of graphene oxide magnetic nanocomposites for the removal of tetrabromobisphenol A,” *Front. Environ. Sci. Eng.*, vol. 7, no. 3, pp. 442–450, 2013.
- [63] Q. Han, Z. Wang, J. Xia, S. Chen, X. Zhang, and M. Ding, “Facile and tunable fabrication of Fe₃O₄/graphene oxide nanocomposites and their application in the magnetic solid-phase extraction of polycyclic aromatic hydrocarbons from environmental water samples,” *Talanta*, vol. 101, pp. 388–395, 2012.
- [64] U. Schwertmann and R. M. Cornell, “Magnetite,” in *Iron Oxides in the Laboratory: preparation and characterization*, Second., U. Schwertmann and R. M. Cornell, Eds. Weinheim, New york, Chichester, Brisbane, Singapore, Toronto: Wiley-VCH Verlag GmbH & Co. KGaA, 2000, pp. 135–140.
- [65] C. Carl, I. Ovid’ko, S. Seal, and S. Veprek, “Stability of structural nanocrystalline materials – grain growth,” in *Structural Nanocrystalline Materials: Fundamentals and Applications*, 1st ed., Edinburgh: Cambridge University press, 2007, pp. 93–133.
- [66] C. Namasivayam and K. Kadirvelu, “Uptake of mercury (II) from wastewater by activated carbon from an unwanted agricultural solid by-product: coirpith,” *Carbon N. Y.*, vol. 37, no. 1, pp. 79–84, 1999.
- [67] L. Largetitte and R. Pasquier, “A review of the kinetics adsorption models and their application to the adsorption of lead by an activated carbon,” *Chem. Eng. Res. Des.*, vol. 109, pp. 495–504, 2016.
- [68] S. Y. Lagergren, “Zur theorie der sogenannten adsorption gelöster stoffe,” 24th ed., Handlingar, 1898, pp. 1–39.
- [69] K. V. Kumar, “Linear and non-linear regression analysis for the sorption kinetics of methylene blue onto activated carbon,” *J. Hazard. Mater.*, vol. 137, no. 3, pp. 1538–1544, 2006.
- [70] Z. Aksu, “Application of biosorption for the removal of organic pollutants: A review,” *Process Biochem.*, vol. 40, no. 3–4, pp. 997–1026, 2005.
- [71] Y. S. Ho and G. McKay, “Pseudo-second order model for sorption processes,” *Process Biochem.*, vol. 34, no. 5, pp. 451–465, 1999.
- [72] S. . Elovich and O. . Larinov, “Theory of adsorption from solutions of non electrolytes on solid (I) equation adsorption from solutions and the analysis of its simplest form, (II) verification of the equation of adsorption isotherm from solutions,” *Izv. Akad. Nauk. SSSR, Otd. Khim. Nauk*, vol. 2, no. 2, pp. 209–216, 1962.
- [73] I. Langmuir, “The adsorption of gases on plane surfaces of glass, mica and platinum,” *J. Am. Chem. Soc.*, vol. 40, no. 9, pp. 1361–1403, 1918.

- [74] S. J. Allen, G. McKay, and J. F. Porter, "Adsorption isotherm models for basic dye adsorption by peat in single and binary component systems," *J. Colloid Interface Sci.*, vol. 280, no. 2, pp. 322–333, 2004.
- [75] L. C. Lin, J. K. Li, and R. S. Juang, "Removal of Cu(II) and Ni(II) from aqueous solutions using batch and fixed-bed ion exchange processes," *Desalination*, vol. 225, no. 1–3, pp. 249–259, 2008.
- [76] L. K. Koopal, W. H. Van Riemsdijk, J. C. M. De Wit, and M. F. Benedetti, "Analytical isotherm equations for multicomponent adsorption to heterogeneous surfaces," *J. Colloid Interface Sci.*, vol. 166, no. 1, pp. 51–60, 1994.
- [77] K. K. H. Choy, J. F. Porter, and G. McKay, "Langmuir isotherm models applied to the multicomponent sorption of acid dyes from effluent onto activated carbon," *J. Chem. Eng. Data*, vol. 45, no. 4, pp. 575–584, 2000.
- [78] F.-S. Zhang, J. O. Nriagu, and H. Itoh, "Mercury removal from water using activated carbons derived from organic sewage sludge," *Water Res.*, vol. 39, no. 2–3, pp. 389–395, 2005.
- [79] D. M. Ruthven, "Adsorption, Fundamentals," in *Kirk-Othmer Encyclopedia of Chemical Technology*, vol. 1, John Wiley & Sons, Inc., 2001, pp. 582–617.
- [80] The MathWorks, "MATLAB 2015b." The MathWorks, Natick, 2015.
- [81] C. Chapa Gonzalez, C. A. Martínez Pérez, A. Martínez Martínez, I. Olivas Armendáriz, O. Zavala Tapia, A. Martel-Estrada, and P. E. García-Casillas, "Development of antibody-coated magnetite nanoparticles for biomarker immobilization," *J. Nanomater.*, vol. 2014, 2014.
- [82] M. Cano, K. Sbargoud, E. Allard, and C. Larpent, "Magnetic separation of fatty acids with iron oxide nanoparticles and application to extractive deacidification of vegetable oils," *Green Chem.*, vol. 14, no. 6, p. 1786, 2012.
- [83] Bruker, "X-ray Diffraction (XRD) and Scattering," *Products-X-ray Diffraction and Elemental Analysis*, 2017. [Online]. Available: <https://www.bruker.com/products/x-ray-diffraction-and-elemental-analysis/x-ray-diffraction.html>. [Accessed: 10-Apr-2017].
- [84] W.-L. Song, M.-S. Cao, M.-M. Lu, J. Liu, J. Yuan, and L.-Z. Fan, "Improved dielectric properties and highly efficient and broadened bandwidth electromagnetic attenuation of thickness-decreased carbon nanosheet/wax composites," *J. Mater. Chem. C*, vol. 1, no. 9, p. 1846, 2013.
- [85] P. Ilieva Girginova, "Novel magnetic materials: from coordination compounds to nanomaterials," University of Aveiro, 2009.
- [86] M. Shen, H. Cai, X. Wang, X. Cao, K. Li, S. H. Wang, R. Guo, L. Zheng, G. Zhang, and X. Shi, "Facile one-pot preparation, surface functionalization, and toxicity assay of APTS-coated iron oxide nanoparticles," *Nanotechnology*, vol. 23, no. 10, p. 105601, 2012.
- [87] N. Chomchoey, D. Bhongsuwan, and T. Bhongsuwan, "Magnetic Properties of Magnetite Nanoparticles Synthesized by Oxidative Alkaline Hydrolysis of Iron Powder," vol. 971, no. October 2015, pp. 963–971, 2010.

- [88] L. M. Malard, M. A. Pimenta, G. Dresselhaus, and M. S. Dresselhaus, "Raman spectroscopy in graphene," *Phys. Rep.*, vol. 473, no. 5–6, pp. 51–87, 2009.
- [89] A. C. Ferrari, J. C. Meyer, V. Scardaci, C. Casiraghi, M. Lazzeri, F. Mauri, S. Piscanec, D. Jiang, K. S. Novoselov, S. Roth, and A. K. Geim, "Raman spectrum of graphene and graphene layers," *Phys. Rev. Lett.*, vol. 97, no. 18, pp. 1–4, 2006.
- [90] D. Yang, A. Velamakanni, G. Bozoklu, S. Park, M. Stoller, R. D. Piner, S. Stankovich, I. Jung, D. A. Field, C. A. Ventrice, and R. S. Ruoff, "Chemical analysis of graphene oxide films after heat and chemical treatments by X-ray photoelectron and Micro-Raman spectroscopy," *Carbon N. Y.*, vol. 47, no. 1, pp. 145–152, 2009.
- [91] M. Matsui, S. Todo, and S. Chikazumi, "Magnetization of low temperature phase Fe_3O_4 ," *J. Phys. Soc. Japan*, vol. 43, no. 1, pp. 47–52, 1977.
- [92] A. R. Muxworthy and E. McClelland, "Review of the low-temperature magnetic properties of magnetite from a rock magnetic perspective," *Geophys. J. Int.*, vol. 140, no. 1, pp. 101–114, 2000.
- [93] R. M. Cornell and U. Schwertmann, *The Iron Oxides: Structure, Properties, Reaction, Occurrences and Uses*, 2nd ed. Wiley-VCH Verlag GmbH & Co. KGaA, 2003.
- [94] X. Batlle and A. Labarta, "Finite-size effects in fine particles : magnetic and transport properties," *J. Phys. D. Appl. Phys.*, vol. 15, no. 35, pp. R15–R42, 2002.
- [95] N. Takeno, "Atlas of Eh-pH diagrams Intercomparison of thermodynamic databases," *National Institute of Advanced Industrial Science and Technology Tokyo*, no. 419. Tokyo, p. 285, 2005.
- [96] D. Podstawczyk, A. Dawiec, A. Witek-Krowiak, and K. Chojnacka, "New Trends in Microbial Biosorption Modeling and Optimization," in *Handbook of Metal-Microbe Interactions and Bioremediation*, 1st ed., S. Das and H. R. Dash, Eds. London: CRC Press-Taylor and Francis Group, 2017, pp. 173–199.
- [97] P. Sharma, G. Singh, and R. Tomar, "Synthesis and characterization of an analogue of heulandite: Sorption applications for thorium(IV), europium(III), samarium(II) and iron(III) recovery from aqueous waste," *J. Colloid Interface Sci.*, vol. 332, no. 2, pp. 298–308, 2009.
- [98] D. D. Shao, Q. H. Fan, J. X. Li, Z. W. Niu, W. S. Wu, Y. X. Chen, and X. K. Wang, "Removal of Eu(III) from aqueous solution using ZSM-5 zeolite," *Microporous Mesoporous Mater.*, vol. 123, no. 1–3, pp. 1–9, 2009.
- [99] A. C. Texier, Y. Andrès, C. Faur-Brasquet, and P. Le Cloirec, "Fixed-bed study for lanthanide (La, Eu, Yb) ions removal from aqueous solutions by immobilized *Pseudomonas aeruginosa*: Experimental data and modelization," *Chemosphere*, vol. 47, no. 3, pp. 333–342, 2002.
- [100] Z. Guo, Y. Li, S. Pan, and J. Xu, "Fabrication of Fe_3O_4 @cyclodextrin magnetic composite for the high-efficient removal of Eu(III) ," *J. Mol. Liq.*, vol. 206, pp. 272–277, 2015.
- [101] R. Akkaya, "Terbium adsorption onto polyhydroxyethylmethacrylate-hydroxyapatite composite and its modified composition by phytic acid," *Desalin. Water Treat.*, vol.

- 52, no. 7–9, pp. 1440–1447, 2014.
- [102] A. D. Site, “Factors Affecting Sorption of Organic Compounds in Natural Sorbent / Water Systems and Sorption Coefficients for Selected Pollutants . A Review Factors Affecting Sorption of Organic Compounds in Natural Sorbent Õ Water Systems and Sorption Coefficients fo,” *J. Phys. Chem*, vol. 187, no. 1, pp. 187–253, 2001.
 - [103] Xcel Energy, “Ashland Lakefront Sediment Remediation.” Xcel Energy Company, Wisconsin, p. 2012, 2012.
 - [104] “Dry mining,” *McGraw-Hill Dictionary of Scientific & Technical Terms*, 2003. [Online]. Available: <https://goo.gl/hWBh1z>. [Accessed: 30-Apr-2017].
 - [105] R. Mitra and S. Saydam, “Surface Coal Mining Methods in Australia,” in *Mining Methods*, P. T. O. Onargan, Ed. Wales: InTech, 2012.
 - [106] J. L. Jambor, “Gangue mineralogy,” *Can. Mineral.*, vol. 11, pp. 402–413, 1971.
 - [107] Lucideon, “Inductively Coupled Plasma Optical Emission Spectroscopy (ICP-OES Analysis),” *Testing & Characterization*, 2017. [Online]. Available: <https://goo.gl/8IJFRb>. [Accessed: 08-May-2017].

Appendices

A- Magnetic nanocomposite fabrication

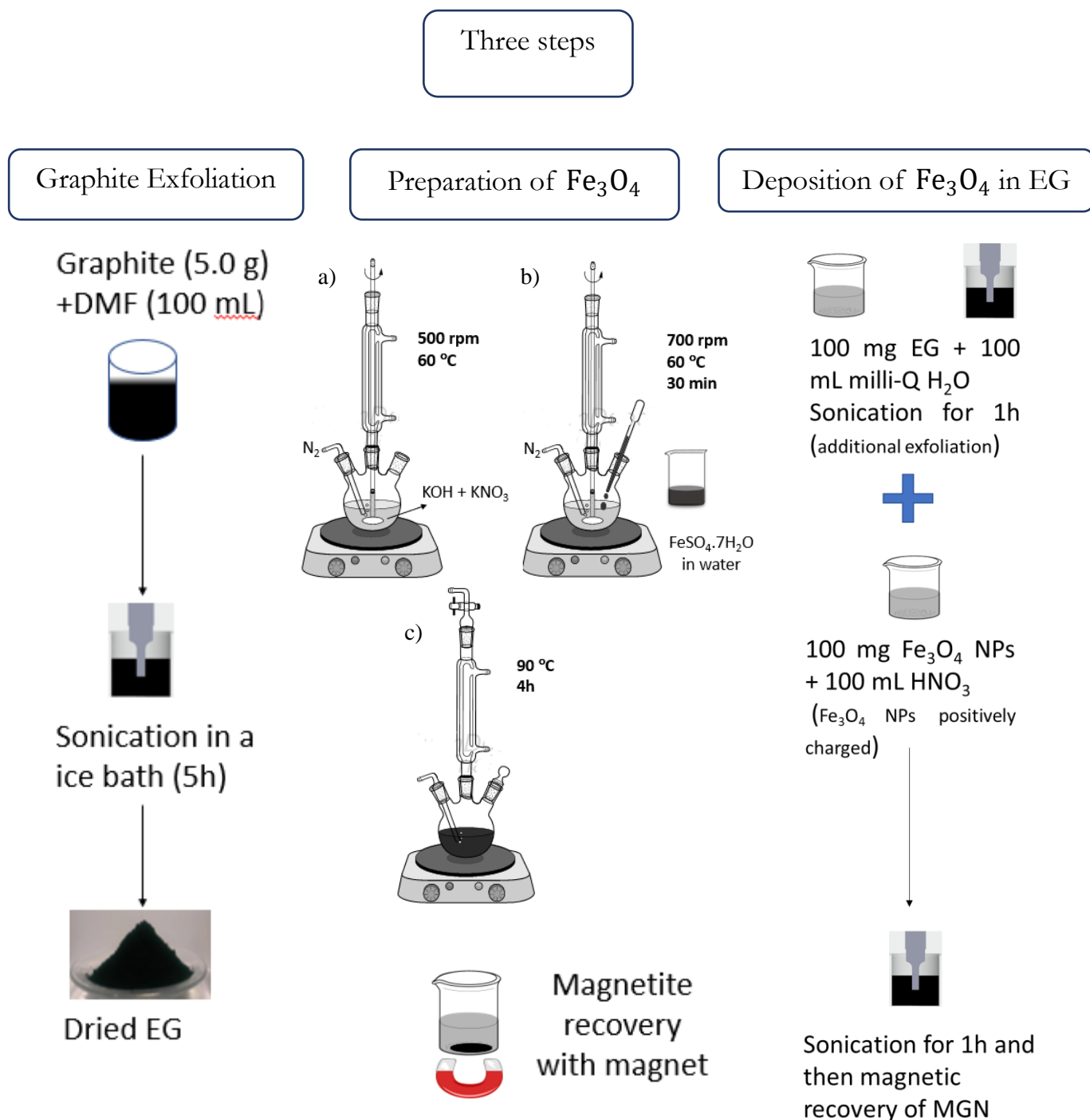


Figure A. 1 - Preparation scheme of magnetic graphene based nanocomposite.

B- Adsorption experiments

- a) 500 mL of Ln^{3+} solution
(0.1 mg L^{-1})

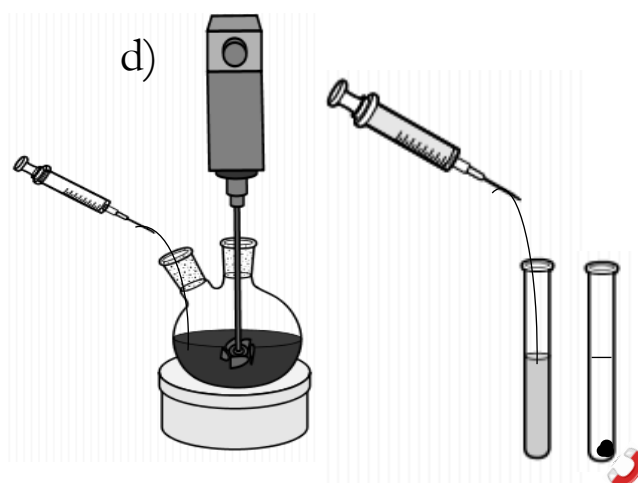
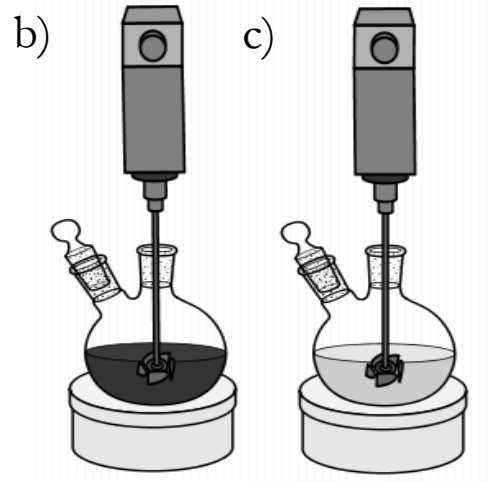


Figure B. 1 - Assembly scheme of adsorption experiments. a) fixed volume of lanthanides solution (500 mL), in 1000 mL two-necked round bottom flask; b) Ln^{3+} solution with MG-bN; c) blank; d) sample collection for ICP-OES.